APPLYING NANOSCALE SCIENCE TO LI-ION BATTERY AND MEMBRANE
TRANSPORT

By

NAICHAO LI

This document is dedicated to my parents, General Keguan Li and Guangxia Zou; my wife, Jing Sun; and my son Xingyue Li.

ACKNOWLEDGMENTS

TABLE OF CONTENTS

CHAPTER

1   INTRODUCTION TO TEMPLATE SYNTHESIS 1

2   HIGH-RATE, HIGH-CAPACITY, NANOSTRUCTURED TIN-BASED ANODE

LIST OF TABLES

LIST OF FIGURES

Abstract of Dissertation Presented to the Graduate School
of the University of Florida in Partial Fulfillment of the
Requirements for the Degree of Doctor of Philosophy

APPLYING NANOSCALE SCIENCE TO LI-ION BATTERY AND MEMBRANE
TRANSPORT

By

Naichao Li

December 2003

Chair: Charles R. Martin
Major Department: Chemistry

This dissertation provides background information on nanoscale science, the
template synthesis of nanomaterials, and its application to Li-ion battery and membrane
transport. My work has shown that compared with conventional thin-film electrodes with
the same mass, the template-synthesized SnO_2 nanofibers and the nanoporous carbon-
honeycomb have much higher rate capability and cycling performance as Li-ion battery
anodes. This is because the high-rate capacity of Li-ion battery is limited by slow solid-
state Li^+ diffusion in electrode materials, and the nanostructured electrodes decrease the
distance that Li^+ must diffuse in the solid state. Furthermore, the surface area of the
nanostructured electrode was larger, making the effective current-density during
discharge smaller than that for a conventional electrode. Better cycling performance was
achieved because the spaces between the nanostructures of electrode materials could
accommodate the volume changes due to Li^+ insertion and extraction through the
electrode materials.

In an effort to combine the advantages of both nanostructured electrodes and all-solid-state Li-ion batteries, a nanostructured all-solid-state Li-ion battery was investigated. This battery was designed to use the carbon honeycomb as the anode and the substrate; the surface and the inner walls of the carbon honeycomb were then covered with an ultrathin electrochemically polymerized poly(phenylene oxide) (PPO) film, which was used as the solid electrolyte. The PPO film was very thin (0.5 – 1.9 nm) and could be easily deposited into the inner walls of the carbon honeycomb. PPO film was only conductive to cations (e.g., Li^+) after sulfonation.

My research also showed that O_2 plasma etching could be used to prepare not only the carbon honeycomb anode but also nanostructured conical pores in polymeric membranes. Conical pore embedded membranes can be used for enhanced membrane transport and resistive-pulse sensing of particles such as molecules and ions. The plasma etch method provides a simple and convenient route for preparing conical-nanopore membranes.

INTRODUCTION TO TEMPLATE SYNTHESIS

Introduction

Nanoscience is one of the most important research and development frontiers in modern science.[1] In its most simplistic sense, nanoscience is the science of small particles of materials. Such small particles are of interest from a fundamental viewpoint because the properties of a material (such as its melting point, and its electronic and optical properties) change when the size of the particles that make up the material become nanoscopic. With new opportunities for technological and commercial development, the importance of nanoparticles has been shown or proposed in areas such as microelectronics, coatings and paints, and biotechnology.

One current commercial application involves using Au nanoparticles as visual indicators in over-the-counter medical diagnostic kits.[2] This is possibly because macroscopic Au has only one color (gold); but nanoparticles of Au can show essentially all of the colors of the rainbow, depending on the size and shape of the nanoparticle.[3] Furthermore, the intensity of the optical absorption of Au nanoparticles is extraordinarily strong, which means that when suspended in a solution or deposited onto a surface, the naked eye can detect a very small quantity of these particles. These properties make Au particles ideally suited as visual indicators.

Some of the most important applications of micro- and nanoparticles are in the fields of biomedical sciences and biotechnology. It has been shown that nanoparticles can be used as vehicles for enzyme encapsulation,[4] DNA transfection,[5-7] biosensors,[8-10]

1

and drug delivery.[11-13] For example, drugs can be incorporated into nanospheres that are composed of a biodegradable polymer; and this allows for the controlled release of the drug as the nanospheres degrade.[11-12]

Spherical nanoparticles have been widely used because they are easier to make than other shapes. However, nanotubes (hollow cylindrical nanoparticles) are also finding increasing applications. Examples of nanotubes include organosilicon polymer nanotubes,[14] self-assembling lipid microtubes,[15-19] fullerene carbon nanotubes,[20-23] template-synthesized nanotubes,[24-27] and peptide nanotubes.[28-31] Compared with spherical nanoparticles, nanotubes show some interesting characteristics for biotechnological applications. First, nanotubes have large inner volumes (relative to the dimensions of tube) that can be filled with any desired chemical or biochemical species, ranging in size from small molecules to proteins,[24,25] second, nanotubes have distinct inner and outer surfaces that can be chemically or biochemically funtionalized,[24] finally, nanotubes have open mouths that provide access to the inner surfaces and allow incorporation of species into the tubes. Although there is no clear distinction between nano and micro, it is generally accepted that if a tube has at least one dimension of 100 nm or less, it is called a nanotube.

One of the well-investigated types of nanotubes is the carbon or fullerene nanotube. It was reported that a reactive molecule could be attached to the sidewalls of single-walled fullerene nanotubes by a simple noncovalent route.[32-36] This reactive molecule was then used to attach proteins to the walls of nanotubes. It has also been suggested that Fullerene nanotubes might be useful in the area of microelectronics.[23, 37-39] It is widely believed that the current lithographic technology will reach its limit during the

next decade. To further miniaturize electronic circuits so that an increasing number of circuits can be accommodated on a single chip, fullerene nanotubes are being investigated. This is because such nanotubes are small, and depending on the structure the nanotubes can have electronic properties similar to metals or semiconductors.[22,37,38] It was reported that components of electronic circuits can be made using fullerene nanotubes.[23,32,33]

Nanomaterials can be synthesized using different techniques. The primary concern of this dissertation is template synthesis, which is a very versatile method for preparing nanomaterials. This chapter provides the background information on template synthesis and its applications to energy production and sensors.

Background

Template Synthesis

Template synthesis is a general method for preparing nanomaterials.[3,40] This method entails the synthesis or deposition of a desired material within the cylindrical and monodisperse pores of a nanoporous membrane or other solid. Depending on the membrane and synthetic method used, the obtained nanomaterials can be solid nanofibers or hollow nanotubes. There are a variety of interesting and useful characteristics associated with template synthesis. Probably the most useful feature of this method is that it is extremely general with regard to the types of materials that can be prepared. We (and others) have used this method to prepare nanofibers and nanotubes composed of metals,[26, 27, 41-49] polymers,[50-53] semiconductors,[54, 55] carbons,[56-58] and Li^+ intercalation materials.[59-61] It is also possible to prepare composite nanostructures, both concentric tubular composites, where an outer tube of one material surrounds an inner tube of another,[62, 63] and segmented composite nanowires.[64] In addition, nanostructures with

extraordinarily small diameters can be prepared. For example, conductive polymer nanofibers with diameters of 3 nm have been prepared.[65] It would be difficult to make nanofibers with diameters this small by lithographic methods. Finally, template synthesized nanostructures can be assembled into a variety of architectures. The nanostructures can remain inside the pores of the template membrane; or they can be freed from the template membrane and collected by filtration. Alternatively, if the nanostructure-containing membrane is attached to a surface and the membrane is removed, an ensemble of micro- or nano-structures that protrude from the surface like the bristles of a brush can be obtained.
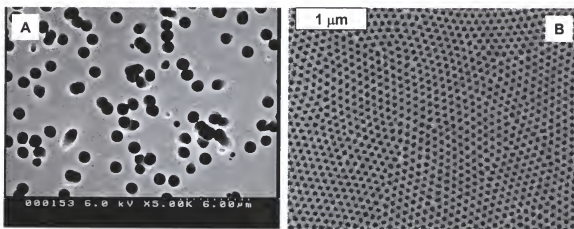
Figure 1-1. Scanning electron micrographs of template membranes. A) Commercially available polycarbonate membrane of 1 μm pore-diameter. B) Alumina membrane of 60 nm pore-diameter prepared in our laboratory.

Template membranes

Two commonly used templates are organic track-etched polycarbonate filters (membranes) and inorganic Al_2O_3 membranes. Track-etched polycarbonate membranes (Figure 1-1A) are produced through a process,[66] which entails bombarding a solid material (e.g., polycarbonate membrane) with a collimated beam of high-energy nuclear fission fragments, to create nearly parallel damage tracks in the film. The damage tracks

are then etched into monodisperse cylindrical pores, by exposing the film to a concentrated solution of base.[66] The diameter of the pores obtained is determined by the etching time and etching solution temperature. The density of pores is determined by the exposure time to the fission-fragment beam. Track-etched membranes such as polycarbonate membranes with pore diameters ranging from 10 nm to 20 μm, and a density as high as 6×10^8 pores cm^{-2} of membrane surface area are commercially available (e.g., Nuclepore, SPI-Pore, Poetics, Osmonics, and Whatman). Because of the random nature of the pore-production process, the angle between the pore direction and the surface normal can be as large as 34°.[67] As a result, a number of pores may actually intersect within the membrane.

Porous Al_2O_3 membranes are produced *via* the anodization of Al metal in an acidic solution.[68] These membranes contain cylindrical pores of uniform diameter arranged in a hexagonal array (Figure 1-1B). Unlike the track-etched polycarbonate membranes, the pores in Al_2O_3 membranes are parallel to the surface normal, and they do not intersect inside the membranes. The Al_2O_3 membranes are commercially available (Whatman, Clifton, New York) in a limited number of pore diameters. However, our research group routinely prepares Al_2O_3 membrane with a broad range of pore diameters.[69,70] The pore diameters of the obtained membranes can be as high as 200 nm and as small as 5 nm.

Other nanoporous materials can also be used as template membranes. One example is nanochannel array glass with a pore diameter as small as 33 nm and pore densities as high as 3×10^{10} pores cm^{-2}.[71] Another example is mesoporous zeolite.[72] Nanoscopic pores in a protein derived from a bacterium and arrays of polypeptide tubes have also

been used.[73,74] Qzin and Schollhorn reviewed a wide variety of nanoporous solids that can be used as template materials.[75,76]

Controlling the pore diameters of template membranes

The pore diameter of polycarbonate and Al_2O_3 membranes can be controlled easily by Au electroless plating. That means one can choose a membrane with a certain initial pore diameter, and then this diameter can be reduced by simply depositing Au nanotubes within the pores of the membrane. This electroless plating method has been described previously.[45,77] In brief, the template membrane is first "sensitized" by immersing into a $SnCl_2$ solution, which results in deposition of Sn(II) onto all of the membrane's surfaces (pore walls and membrane faces). The sensitized membrane is then immersed into a $AgNO_3$ solution; and a surface redox reaction occurs (Equation 1-1) that yields nanoscopic metallic Ag particles on the membrane surfaces. The redox reaction is given by

$$Sn(II)_{surf} + 2\ Ag(I)_{aq} \longrightarrow Sn(IV)_{surf} + 2\ Ag(0)_{surf} \qquad (1-1)$$
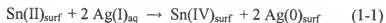
where subscripts surf and aq in Equation 1-1 denote species adsorbed to the membrane surfaces and species dissolved in solution, respectively. The membrane is then immersed into a commercial Au plating solution and a second surface redox reaction occurs, to yield Au nanoparticles on the surfaces (Equation 1-2).

$$Au(I)_{aq} + Ag(0)_{surf} \longrightarrow Au(0)_{surf} + Ag(I)_{aq} \qquad (1-2)$$
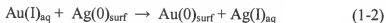
These surface-bound Au nanoparticles are good autocatalysts for the reduction of Au(I) to Au(0) using formaldehyde as the reducing agent. As a result, Au deposition begins at the pore walls, and Au nanotubes are obtained within the pores.[26,27,44-46,78,79] In addition, the faces of the membrane become coated with thin Au films. These surface films do not, however, block the mouths of the nanotubes, and there are open nanoscopic

channels running from one face of the membrane to the other. By controlling the electroless plating time, the inside diameter of these nanotubes can be controlled at will, down to molecular dimensions.[45]

Measuring the pore diameter of membranes

The pore diameter can be obtained from scanning electron microscopic (SEM) images of the membrane surface. However due to the resolution limitation of the SEM, this method can only be used for membranes with a pore diameter of more than 30 nm. A gas transport method is used by our group to obtain a measure of the pore diameter for membranes containing small pores.[45] Briefly, the membrane containing either small diameter pores or tubes is placed in a gas-permeation cell, and the upper and lower half-cells are evacuated. The upper half-cell is then pressurized, typically to 20 psi with H_2, and the pressure-time transient associated with leakage of H_2 through the nanotubes or pores is measured using a pressure transducer in the lower half-cell. The pressure-time transient is converted to gas flux (Q, mol s^{-1}), which is related to the radius of the nanotubes (r, cm) *via* Equation 1-3[45,80]

$$Q = 4/3(2\pi/MRT)1/2(nr^3\Delta P/l) \qquad (1-3)$$

where ΔP is the pressure difference across the membrane (dynes cm^{-2}); M is the molecular weight of the gas; R is the gas constant (erg K^{-1} mol^{-1}); n is the number of nanotubes in the membrane sample; l is the membrane thickness (cm); and T is the temperature (K).

In using Equation 1-3, we assume: (i) that we know the number of nanotubes or pores in the membrane sample; (ii) that the nanotubes or pores have a constant inside diameter down their entire length; and (iii) that the mechanism of gas transport through

the membrane is Knudsen diffusion.[81] The validity of these various assumptions have been discussed in detail in a review article.[81]

Applying Template Synthesized Nanomaterials to Li-Ion Battery

Energy, the environment and information technology have become key resources for the 21st century as they deeply influence our daily life. The search for power sources has taken place since the beginning of the civilization. This search resulted in the finding and application of fossil fuel, nuclear energy, solar energy, etc. However this search has not stopped yet, because the need for more efficient, convenient, pollution-free and safe energy sources is increasing. Currently the internal combustion engine is a major consumer of fossil fuel, consuming about 1/3 of the annual total demand for energy. This causes huge concerns over global warming and air pollution.[82] As a result, energy storage devices such as batteries have been developed. They include the Li-ion battery, nickel and metal hydride battery, and lead acid and nickel cadmium batteries.

The battery industry has seen enormous growth over the past few years in portable recharge-battery packs. The majority of this surge can be attributed to the widespread integration of cell phones, laptop computers and other wireless electronics. While wireless applications are experiencing a rapid growth, other applications such as medical, portable power tools, and military applications are experiencing mixed growth rates. Despite the global economic slowdown, the world-wide market for battery sales in 2001 was worth nearly $39 billion. The rechargeable sector represented approximately two-thirds of the revenue ($26 billion).[83] The volume and weight energy densities of a variety of rechargeable batteries are shown in Table 1-1.[84] We can find among all the rechargeable batteries, the Li-ion battery has the highest energy density. The Li-ion

battery is expected to be the main choice for most of the higher-end portable electronic equipment, and to dominate the rechargeable battery market through 2005.[83]

Table 1-1. Characteristics of rechargeable batteries

Battery type	Nominal voltage (V)	Energy density	
		In weight (Wh g^{-1})	In volume (Wh l^{-1})
Pb-acid	2.0	35	70
Ni-Cd	1.2	40	100
Ni-MH	1.2	40	100
Ag-Zn	1.5	110	220
Li-ion	3.6	125	440

The Li-ion battery was first commercialized in 1990 by Sony Energetic Inc.[85] It is a rechargeable battery and uses Li^+ intercalation compounds as the cathode and anode. Unlike conventional rechargeable batteries that are based on chemical reactions, the working of Li-ion battery is based on intercalation reactions. Taking an example of a Li-ion battery with carbon as the anode material and $LiCoO_2$ as the cathode material, during the charging process, Li ions are extracted from the $LiCoO_2$ cathode (Equation 1-4) and inserted into the carbon anode (Equation 1-5); during the discharging process, Li ions are extracted from the carbon anode (Equation 1-4) and inserted into the $LiCoO_2$ cathode (Equation 1-5).

$$\text{Anode: } 6\,C + Li^+ + e^- \underset{\text{discharge}}{\overset{\text{charge}}{\rightleftharpoons}} LiC_6 \qquad (1\text{-}4)$$

$$\text{Cathode: } LiCoO_2 \underset{\text{discharge}}{\overset{\text{charge}}{\rightleftharpoons}} CoO_2 + Li^+ + e^- \qquad (1\text{-}5)$$
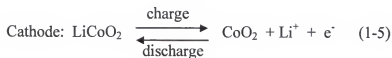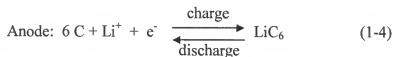
Despite success in the commercial marketplace, an enormous international effort is now aimed at improving Li-ion battery technology. This effort focuses on developing improved anodes,[86-88] cathodes,[89-91] and electrolytes.[92-95] An area where improvement is

critically needed concerns the rate capability of the battery, that is, its ability to deliver large capacity when discharged at a high discharge rate. An improvement in the rate capabilities of Li-ion batteries is required because there are increasing needs for high-power pulses in communications and remote sensing devices.

Figure 1-2. Scanning electron micrograph of the template synthesized $LiMn_2O_4$ nanotubes of 150 nm outside-diameter.

It is now well established that the limitation in the rate capability of a conventional Li-ion batteries is caused by slow solid-state diffusion of Li^+ within the electrode materials.[57, 59, 60,61, 96] As a result, there is tremendous research interest in the development of nanostructured Li-ion battery electrodes.[57,59-61,97-104] Nanostructured electrodes can overcome the problem of slow Li^+ diffusion because the distance that Li^+ must diffuse in the solid-state is dramatically decreased. The nanostructured electrodes can be Sn-based nanoparticles,[97,98] fullerene nanotubes,[99,100] vanadium oxide nanotubes,[101,102] as well as highly porous aerogels.[103,104] In our research group, we have been exploring the use of the template synthesis method to prepare nanofibers or nanotubes of Li^+ insertion materials, which protrude from an underlying current-collector surface like the bristles of a brush (Figure 1-2). The materials synthesized were carbon,[57]

$LiMn_2O_4$,[60] V_2O_5, and TiS_2.[59,61] In all cases, the rate capabilities were significantly improved, relative to thin-film-control electrodes composed of the same material.

Applying the Nanotube Membranes for Resistive-Pulse Sensing

Resistive-pulse sensing is a technique based on an electrochemical cell in which a piece of membrane with a single aperture separates two ionically conductive salt solutions. An electrode is placed into each salt solution, and a constant DC voltage is applied across the membrane. An analyte species whose diameter is comparable to the inside diameter of the aperture is then introduced into one of the salt solutions. When the analyte enters the aperture it partially occludes the pathway for ionic conduction and the ionic current through the aperture decreases. Depending on the device, this change in current can be used to size, identify, and determine the concentration of the analyte species.[105]

The classical example of a resistive-pulse sensor or a stochastic sensor is theCoulter counter,[106,107] a commercially available device used to count and size biological cells and colloidal particles. It can measure particles with diameters ranging from as small as 400 nm to as large as 1 mm.[106,107] This is in agreement with the Beckman Coulter product literature, which states that an aperture can be used to detect particles in the range from 2% to 60 % of the aperture diameter.[107] For stochastic sensing, the height of the produced current pulse is proportional to the particle size, and the number of current pulses is proportional to the number of particles in the solution. Obviously, molecule and ion sensing is possible if the aperture used in the sensing element is of molecular dimensions. Fortunately such molecule-sized apertures can be borrowed from Mother Nature-protein channels and pores. Synthetic analogues of such nanoscopically sized structures can also be used.[105]

Although single-channel sensing is of great current interest, it was first achieved more than 30 years ago in 1970. Hladky and Haydon reported the first definitive single-channel recordings from a bilayer of glycerol mono-oleate containing a low concentration of gramicidin A.[108] They observed the opening and closing of individual channels formed by gramicidin A. A variety of biological channel systems can be used for resistive-pulse sensing. They can be, α-hemolysin (α-HL) channels, acetylcholine receptors, other ligand-gated channels, and K^+ channels.[105] The use of unmodified biological channels as sensor elements has produced very promising results. However the full promise of proteins in sensors lies in the modification of their properties by "protein engineering", a term that encompasses a multitude of manipulations.[109]

The most interesting experimental results of stochastic sensing using staphylococcal α-HL protein channel have been reported by Bayley's research group.[110,111] In their case, the channel formed by wild-type α-HL consists of seven identical subunits arranged around a central axis; the transmembrane part of the lumen is a β-barrel with two antiparallel strands contributed by each subunit; the extramembraneous domain contains a large cavity that houses the transmembrane domain during the assembly process, but which is available for engineering in the assembled channel. Taking an example of the analysis of organic molecules, when non-covalent adapters such as β-cyclodextrin is lodged in the lumen of the α-HL channel. β-cyclodextrin remains capable of binding the same organic molecules that it binds when free in solution; these binding events cause current fluctuations that permit the qualification and the identification of the molecules.

One disadvantage of current generation of stochastic sensors is their lack of durability, which confines their use to the laboratory. Several crucial advances will be required to make a practical device. We and other research groups are interested in making abiotic stochastic sensing devices. We believe that a membrane containing a single conical nanopore or nanotube might function as an abiotic stochastic sensor. The conical nanopore or nanotube shape is essential because the membranes we will use have thickness between 2 and 10 μm. This means that at any time there might be hundreds of analyte molecules in the pore. But we only want to detect them one at a time. With a conical nanopore this is possible because in principle only the molecule blocking the small diameter opening of the pore is detected. My research work has shown that conical nanopore membranes can be easily obtained by just using an O_2-plasma etch method. Compared with the conventional chemical etch method, plasma etching is very simple and convenient.

Applying the Nanotube Membranes for Membrane Transport

There is a long-standing interest in our research group in the area of membrane-based chemical separations and transport.[112-114] This interest led us to undertake a series of fundamental investigations of the transport properties of the gold nanotube membranes. We discovered that by controlling the deposition time, Au nanotubes that had effective inside diameters of molecular dimensions (< 1 nm) were obtained.[27] This suggested that these membranes might be useful as molecular sieves. In principle, molecular sieving is a result of hindered diffusion of the molecules in the Au nanotubes.[115] It is based on the Stokes-Einstein equation that relates the diffusion

coefficient (D_s) to the molecular radius (r_m) for diffusion in free solution (Equation 1-6), it is given by

$$D_s = kT/6\pi\eta\rho r_m \qquad (1\text{-}6)$$

where k is the Boltzmann constant, T is the Kelvin temperature, and η is the viscosity. The denominator $6\pi\eta\rho r_m$ can be thought as a molecular-friction coefficient that determines the resistance to diffusion in the solution. As would be expected, this molecular-friction term increases with increasing size of the molecule and increasing viscosity of the solution.

In the Au nanotube membranes, this molecular-friction coefficient is larger than in free solution because collisions with the nanotube wall increase the frictional drag on the molecules.[116] In addition, the rate of diffusive mass transport in the nanotube is decreased, relative to a contacting solution phase, because of steric reasons.[115] The diffusion of molecules across the nanotube membranes is defined by the Renkin equation (Equation 1-7)[117]

$$D_{tube}/D_{sol} = 1 - 2.104\lambda + 2.09\lambda^2 - 0.95\lambda^5 \qquad (1\text{-}7)$$

where D_{tube}, D_{sol} are the diffusion coefficients of molecules in the nanotube and the solution, respectively. λ is defined as r_m/r_{tube}, in which r_{tube} is the radius of the tube. Equation 1-7 indicates that diffusivity in the nanotube membranes will be lower for larger molecules but higher for smaller molecules.

Molecular sieving experiments in our research group were conducted using a simple U-tube permeation cell, where the membrane to be studied separates the feed and permeate half-cells. The feed half-cell initially contains only water or a salt solution. Passive diffusion drives the permeate molecule from the feed half-cell through the

membrane and into the permeate half-cell. The time course of the transport process is followed by periodically assaying the permeate half-cell for the permeate molecules. It has been demonstrated that the transport flux (Moles transported per permeation minute) of smaller molecule (methyl viologen) is 172 times of that of the larger molecule (tris-bipyridal complex of Ru(II), $Ru(bpy)_3^{2+}$.[27] Molecular sieving could also be extended to biological molecules. We have shown that this allows for controlling protein-transport selectivity on the Au nanotube membranes.[118,119]

Besides showing size-based selectivity, our research work also shows that Au nanotube membranes can show ionic charge-based transport selectivity and that the membranes can be electrochemically switched between anion and cation transporting states.[26] Hence, these membranes can be viewed as universal ion-exchangers. Furthermore, chemical transport selectivity can be introduced into these membranes by chemisorbing thiols to the inside tube walls.[44,45] In this case, the chemisorbed thiol changes the chemical environment within the nanotubes and this, in turn, changes the transport properties of the membrane. For example, membranes modified with hydrophobic thiols selectively transport hydrophobic molecules.[45] Hence, these nanotube membranes can utilize all of the selectivity paradigms (sterics, electrostatics, and chemical interactions) that Mother Nature uses in the design of her exquisitely selective molecule-recognition schemes.

It is interesting to mention that in the cylindrical pores hindered diffusion would occur down the entire the length of the pore. In contrast, in the conical pores hindered diffusion would only be dramatically higher in the conical pores. Hence, for large permeate molecules the conical-pore membranes should yield higher fluxes than the

cylindrical-pore membranes. My research work has shown that conical-pore membranes can be simply prepared using a O_2-plasma etch method, and enhanced ionic transport has be obtained using these membranes.

CHAPTER 2
HIGH-RATE, HIGH-CAPACITY, NANOSTRUCTURED TIN-BASED ANODE

Introduction

As noted previously, template synthesis is a general method for preparing nanomaterials. It entails synthesis of the desired material within the pores of a nanoporous membrane or other solid.[3,40] The membranes employed contain cylindrical pores with uniform and monodisperse diameters that run the complete thickness of the membrane (typically 6 to 10 μm thick). Corresponding cylindrical nanostructures of the desired material are deposited within the pores. Of particular interest to battery research and development, the template method can be used to prepare nanostructures of Li-ion battery electrode materials.[59-61] High-density ensembles of these nanostructures have been prepared, where the nanostructures protrude from a current collector surface like the bristles of a brush.

We have demonstrated that these nanostructured Li-ion battery electrodes have better rate capabilities than conventional electrodes composed of the same materials.[59-61] Better rate capabilities are obtained because the distance over which Li^+ must diffuse in the solid state is dramatically decreased within the nanostructured electrode. Furthermore, the surface area of the nanostructured electrode is larger, making the effective current density during discharge smaller than that for a conventional electrode. Other laboratories have also observed improved rate capabilities for Li-ion battery electrodes prepared from smaller-sized particles and/or high surface-area Li^+-insertion materials.[87,88,103,104,120-123]

Anodes derived from oxides of tin (e.g., SnO_2) have recently been of considerable interest because they can, in principle, store over twice as much Li as graphite.[86,124,125] However, large volume changes occur when Li is inserted and removed from these Sn-based materials, and this causes internal damage to the electrode resulting in loss of capacity and rechargeability.[87,88] Prior work has shown that both the size of the particles constituting the electrode; and the size of the grains within these particles, play critical roles in this unwanted decomposition process. Specifically, electrodes composed of smaller particles and crystallites show better cyclability.[87,88]

This suggests that there might be some fundamental advantage to applying the template synthesis method to Sn-based anode materials. We have used sol-gel template synthesis to prepare nanofibers of SnO_2 within the pores of a nanoporous polycarbonate template membrane.[54] These SnO_2 nanofibers were electrochemically converted to composite Sn/Li_2O nanofibers and the charge/discharge properties of these nanostructured electrodes were investigated.[88] These electrodes can deliver a very high capacity (>700 mAh g^{-1}) at very high discharge rates, and still retain the ability to be discharged and recharged through many cycles. The results of these investigations are described here.

Experimental

Materials

The template membrane used was a commercially available polycarbonate filter (Poretics). The characteristics of this membrane are shown in Table 2-1. $SnCl_2 \cdot 6H_2O$ (Aldrich), ethanol (200 proof, Pharmco), lithium perchlorate (99.99%, Aldrich), diethyl carbonate (99%, Aldrich), ethylene carbonate (battery grade, Ferro Corp) and Platinum foil (2.0 cm x 2.0 cm x 0.005 cm, Aldrich) were used as received. Purified water was

obtained by passing house distilled water through a Millipore, Milli Q water purification system.

Table 2-1. Characteristics of the template membrane and SnO_2 nanofibers

Nominal pore diameter (nm)[a]	Nanofiber diameter (nm)[b]	Nominal pore density (cm^{-2})[a]	Measured pore density (cm^{-2})[c]	Nanofiber density (cm^{-2})[d]	Membrane thickness (μm)[a]
50	110	6×10^8	6×10^8	5×10^8	6

a. As specified by the vendor.
b. measured using TEM.
c. Measured from SEMs of the membrane.
d. Measured from SEMs like that shown in Figure 2-2A.

Preparing the Nanostructured SnO_2 Electrode

Nanostructured electrodes were prepared by immersing the polycarbonate template membrane into a tin oxide-based sol. The sol was prepared by dissolving 0.338 g of $SnCl_2 \cdot 6H_2O$ in a solvent mixture composed of 0.47 mL of ethanol and 0.03 mL of 37% hydrochloric acid to yield a 3 M Sn(II) solution. This solution was aged for 24 hours to yield a very fine white precipitate, which was shown by X-ray diffraction to be SnO_2. Water (0.03 mL) was then added, and over a period of 24 hours the precipitate was resuspended to yield a transparent sol.

A piece of the template membrane was immersed for 24 hours into the sol and then placed on a Pt-foil current collector (area = 1.5 cm^2). Because the membrane at this point was wet, good adhesion with the underlying Pt surface was obtained. The membrane surface was wiped of excess solution using a laboratory tissue, and the solvent was allowed to evaporate in air at *ca.* 80 °C. The polycarbonate template membrane was then burned away with oxygen plasma (200 W, 33 Pa, 1.5 hours). The Plasma System used was a Micro-RIE Series 85 (Technics International). Plasma etching resulted in an

ensemble of cylindrical tin oxide precursor-gel nanostructures protruding from the Pt foil surface like the bristles of a brush. Heat treatment at 440 °C for 2 hours in air was used to convert the precursor gel into cassiterite, syn-SnO_2 (Figure 2-1).
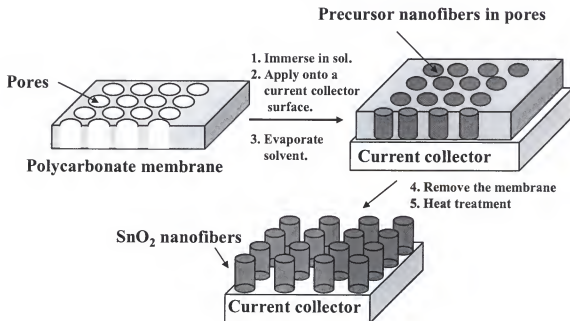
Figure 2-1. Schematic of the SnO_2 nanofiber electrode preparation.

Preparing the SnO_2 Thin-Film-Control Electrode

The SnO_2 control electrode was prepared by dipping a Pt current collector (without a template membrane) into a similar tin oxide-based sol. However, the Sn(II) concentration in this sol was decreased to 1 M in order to lower the viscosity so that a thin film could be obtained. The aging conditions used for the sol were identical to that employed to prepare the nanostructured electrodes, and the heat treatment procedure to yield SnO_2 was also identical.

Characterizing

A Phillips PW 2773/00 powder x-ray diffractometer was used to study the crystal structure of SnO_2 powder, which was obtained using the same sol-gel procedure used to

prepare the nanostructured SnO_2. Scanning electron microscopic (SEM) images were obtained by attaching the Pt foil covered with the protruding SnO_2 nanostructures (or the SnO_2 thin film) to an SEM sample stub with a piece of copper foil tape. The resulting sample was imaged using a Phillips 505 scanning electron microscope. The number of fibers (per cm^2 of current collector surface) was obtained from such images; data from three different images were averaged. Transmission electron microscopic (TEM) images were obtained by removing the nanostructured SnO_2 from the surface of the Pt substrate by scrapping with a razor blade. The liberated nanostructures were dispersed in methanol and a drop of this dispersion was applied to a TEM grid. TEM images were obtained using a JEOL 2000 microscope.

The amount of the nanostructured and thin-film SnO_2 electrodes was obtained *via* inductively coupled plasma (ICP) atomic emission analysis using a Zeeman spectrometer. This was accomplished by dissolving the SnO_2 in 1 M HCl, and determining the Sn^{2+} concentration of the resulting solution. The mass of SnO_2 was calculated from the concentration of Sn^{2+} in the solution. In our prior work on template-synthesized nanostructures, the synthetic methods used yielded surface layers of the electrode material on both faces of the template membrane along with the desired fibers or tubes within the pores of the membrane.[55,59] These surface layers had to be removed prior to dissolution of the template membrane, either for SEM or electrochemical analysis. The method used here to prepare the SnO_2 nanostructures did not produce noticeable SnO_2 surface layers. This greatly decreased the time and labor to prepare samples for these various analyses.

Electrochemical Measurements

Cyclic voltammetric experiments were conducted using a model CV-27 voltammograph (Bioanalytical System Inc.) in conjunction with a Yokogawa 3025 X-Y recorder. Constant current charge/discharge experiments were conducted using an EG&G Princeton Applied Research Model 263 potentiostat/galvanostat in conjunction with a Gateway 2000 computer. A three-electrode cell with nanostructured or thin-film-control electrode as the working electrode and Li foils as counter and reference electrodes was used. The electrolyte was 1 M LiClO$_4$ in a 30:70 (vol.%) mixture of ethylene carbonate and diethyl carbonate. All electrochemical experiments were conducted at room temperature in a glove box filled with argon.

Results and Discussion

Tin Oxide Electrochemistry

The Li$^+$ electrochemistry of the SnO$_2$-based electrodes is interesting because it entails first the irreversible conversion of the tin oxide to metallic tin and then the reversible alloying/dealloying of the Sn with Li.[88]

$$4 \text{ Li}^+ + 4\text{e}^- + \text{SnO}_2 \longrightarrow 2 \text{ Li}_2\text{O} + \text{Sn} \qquad (2\text{-}1)$$

$$x \text{ Li}^+ + x\text{e}^- + \text{Sn} \underset{\text{discharge}}{\overset{\text{charge}}{\rightleftharpoons}} \text{Li}_x\text{Sn} \quad 0 \leq x \leq 4.4 \qquad (2\text{-}2)$$
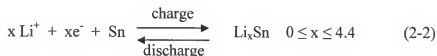
It is this alloying/dealloying process that gives this material its reversible charge storage capacity. In theory as many as 4.4 Li atoms can be stored per atom of Sn which would give the SnO$_2$ anode a maximum theoretical charge storage capacity of 781 mAh g^{-1} *vs.* 372 mAh g^{-1} for graphite. In addition, this charge is stored at high energies, within one volt of the reduction potential for Li$^+$/Li. However, as noted above, Sn undergoes

dramatic volume changes (up to 300%) upon formation of the Li-Sn alloy, which result in internal damage and loss of capacity with cycling.[87,88]

Isidorsson *et al.* have used Mössbauer spectroscopy to study the electrochemical conversion of SnO_2 to Sn.[126] They suggest that the electrochemistry is more complicated than that shown by Equation 2-1 and Equation 2-2. According to the Mössbauer data, SnO_2 is initially intercalated with Li^+ up to an x value of *ca.* 0.1. Between x = 0.1 and 0.2 the SnO_2 is then reduced to SnO; this corresponds to a potential of *ca.* 1.1 V *vs.* Li^+/Li. To date, no electrochemical (e. g. cyclic voltammetric) evidence for this Sn(IV)-to-Sn(II) conversion has been observed.
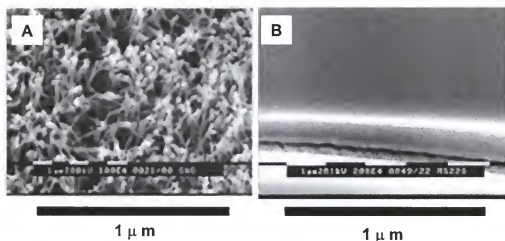
Figure 2-2. Scanning electron micrographs of thin-film and nanostructured electrodes.
A) Template-synthesized nanostructured SnO_2 anode. B) Thin-film-control SnO_2 electrode. Images were obtained before electrochemical cycling.

Characterizing the Nanostructured and Thin-Film SnO_2 Electrodes

Figure 2-2A shows an SEM image of the template-synthesized SnO_2 nanostructures. Fibrous nanostructures that extend the complete thickness of the template membrane are obtained. The number of fibers (per cm^2 of current collector surface) obtained from such images is shown in Table 2-1. SEM was also used to determine the pore density of the membrane. The agreement between the pore density and the fiber

density is reasonably good (Table 2-1); however, the fiber density is always less than the pore density suggesting that some fibers are lost from the current collector surface.

Figure 2-2B shows an SEM image of the thin-film-control electrode. These films are defect free and have a dense and uniform structure. A film thickness of 550 nm was obtained from such images. Because of the dense nature of the thin-film electrode, the area exposed to the electrolyte solution is, to a first approximation, the geometric surface area of the film. Assuming that the fibers are also dense and defect free, it is easy to show from the diameter and number of fibers that the nanostructured electrode has an exposed surface area that is 14 times higher than the thin-film electrode (Table 2-2). As discussed in our previous papers, this higher surface area is one reason the nanostructured electrodes have improved rate capabilities.[59-61]

20 nm
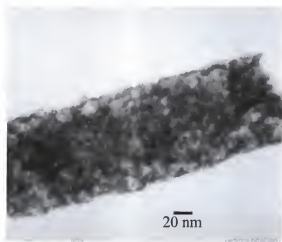
Figure 2-3.   Transmission electron micrograph of a template-synthesized SnO_2 nanofiber. Image was obtained before electrochemical cycling.

Figure 2-3 shows a bright-field TEM image of a single SnO_2 nanofiber. The diameter of the fiber obtained from such images is 110 nm (Table 2-1). As has been observed previously,[127,128] this diameter is significantly greater than the nominal pore diameter. It has been suggested that this occurs because the pore diameter at the surface

of the template membrane is less than that of the pore through most of the thickness of the membrane (i.e., bottleneck pores[27]).[128] Since the nominal pore diameter is obtained *via* SEM of the membrane surface, only the smaller surface pore diameter is seen and reported. Bottleneck pores are obtained because of secondary electron emission from ion impact in the interior of the pore.[128]

Figure 2-4A shows an SEM image of a nanostructured SnO_2 electrode after 800 charge/discharge cycles. Three key differences can be seen relative to the image obtained before cycling (Figure 2-2A). First, the diameter of the fiber is larger after cycling. This is more clearly seen in the post-cycling TEM image shown in Figure 2-4B. This image indicates the diameter increased from 110 nm before cycling to 190 nm after cycling. Second, after cycling there are "bulbs" on the ends of the SnO_2 fibers (Figure 2-4A). Third, in addition to these bulbs, after cycling the sides of the fibers are appreciably roughed.
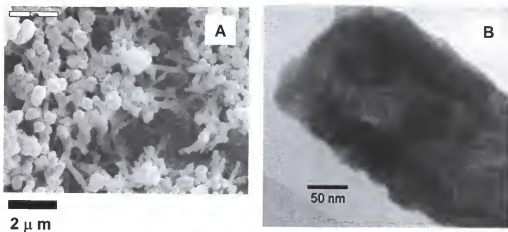
Figure 2-4. Scanning and transmission electron micrographs of the delithiated nanostructured electrode. A) Scanning electron micrograph after 800 charge/discharge cycles at 58 C rate. B) Transmission electron micrograph after 800 charge/discharge cycles at 58 C rate.

All three of these post-cycling features are caused by the volume expansion associated with alloying of the Sn with Li.[87,88] The bulbs on the ends of the fibers are especially interesting. Bulb formation indicates that there is greater volume expansion at the ends of the fibers than along the length of the fibers. Along its length, Li can enter the fibers only through the fiber walls, in a direction normal to the fiber axis. In contrast, at the end of the fiber, Li can not only enter through the fiber wall but also through the fiber end, in a direction parallel to the fiber axis. We believe that this accounts for the greater expansion of the fiber ends resulting in bulb formation.
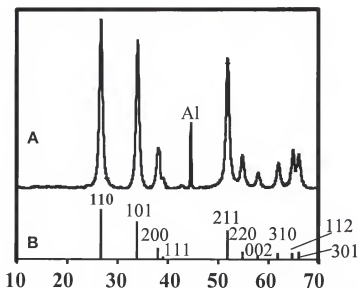
Figure 2-5.   X-ray diffraction patterns of SnO_2. A) SnO_2 powder prepared using the same procedure as the nanostructured electrodes. B) Standard pattern of cassiterite, syn-SnO_2.

In order to compare the electrochemical response characteristics of the nanofibrous and thin-film-control electrodes, the SnO_2 mass for each electrode should be the same. This was accomplished by using a larger area of the fibrous electrode than of the thin-film electrode (Table 2-2). The X-ray diffraction pattern of SnO_2 powder synthesized

using the same procedure as that of the nanofibrous SnO_2 is shown in Figure 2-5A. All peaks are assignable to cassiterite, syn-SnO_2, as indicated by the standard X-ray diffraction pattern in Figure 2-4B (obtained from the American Society for Testing Materials).[129]

Table 2-2. Characteristics of the nanostructured and thin-film SnO_2 electrodes

	Nanofiber diameter (nm)[a]	Film thickness (nm)[b]	Current collector area (cm^2)	Mass of SnO_2 (mg)[c]	Ratio of surface area to geometric area[d]
Nanofiber	110		1.5	0.081	14
Thin film		550	1.2	0.081	1

a. Measured using TEM.
b. Measured using SEM.
c. Obtained from ICP analysis.
d. Calculated from measured fiber diameter and density.

Cyclic Voltammetric Experiments

Figure 2-6A shows the first voltammetric scans of a typical thin-film-control electrode (scan rate = 0.2 mV s^{-1}). The first scan was started at the open-circuit potential (2.5 V), and the scan was reversed at a lower (negative) limit of 0.15 V. The return (positive-going) scan was then reversed at a potential of 0.95 V and the potential was again scanned negatively to 0.15 V. The final positive-going return scan was terminated at 0.95 V. As is typically observed over this potential window;[88,130,131] two primary reduction waves are seen on the first negative scan. One is centered at *ca.* 0.9 V and the other is centered at *ca.* 0.25 V. The reduction wave at 0.9 V corresponds to the irreversible conversion of SnO_2 to Sn and Li_2O (Equation 2-1).[88,130,131] The reduction wave at 0.25 V corresponds to the subsequent alloying of the Sn with Li; and the oxidation wave centered at *ca.* 0.5 V is associated with the dealloying process. These waves provide the reversible capacity for the Sn anode (Equation 2-2).
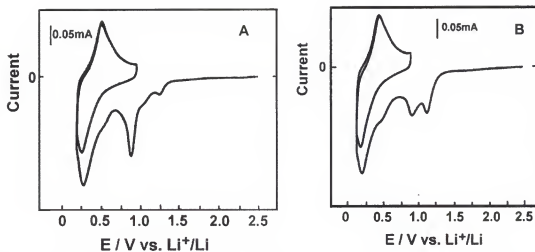
Figure 2-6. Cyclic voltammograms of the thin-film and nanostructured electrodes at a scan rate of 0.2 mV s^{-1}. A) The thin-film-control SnO$_2$ electrode. B) The nanostructured SnO$_2$ electrode.

Careful examination of the cyclic voltammograms in Figure 2-6A shows that there is a small reduction wave (*ca.* 1.25 V) prior to the main SnO$_2$-to Sn(0) reduction wave at 0.9 V and that there is a small shoulder between these two waves. Similar voltammetric features have been observed by Brousse *et al.* and by Panero *et al.*[130, 131] As will be discussed in greater detail below, these features suggest that the Sn(IV)-to-Sn(0) conversion process occurs *via* a series of discrete steps. Figure 2-6B shows the corresponding voltammograms for the nanostructured SnO$_2$ electrode. The reduction wave at 0.25 V and the oxidation wave at 0.5 V remain unchanged, indicating that the alloying/dealloying process is identical for both the thin-film and nanostructured electrodes. However, the irreversible Sn(IV)-to-Sn(0) process for the nanostructured electrode is seen as two clearly resolved peaks instead of the combination of two peaks seen at the thin-film electrode.

As noted above, Isidorsson *et al.* have shown *via* Mössbauer spectroscopy that the reduction of Sn(IV) to Sn(0) occurs in two distinct stages, the reduction of Sn(IV) to

Sn(II) and the subsequent reduction of Sn(II) to Sn(0).[126] We suggest that the two distinct reduction waves seen near 1 V in Figure 2-6B corresponding to these two separate reduction processes. This is supported by the fact that the more positive wave, assigned to the Sn(IV)-to-Sn(II) process, occurs at essentially the same potential as found in the Mössbauer experiment. In addition, the charges associated with these two waves are nearly identical (0.11 coulombs for the more positive wave and 0.13 coulombs for the more negative wave), as would be the case if they correspond to the reduction of Sn(IV) to Sn(II) and the subsequent reduction of the Sn(II) to Sn(0).
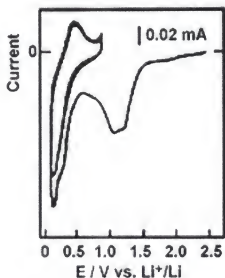
Figure 2-7. Cyclic voltammograms for the thin-film SnO_2 electrode at a scan rate of 0.1 mV s^{-1}

We suggest that the reason two distinct waves are seen at the nanostructured electrode has to do with the very small particle size, which ensures that the entire particle is at equilibrium with the applied potential throughout the voltammetric scan. This means that the entire particle is first converted from Sn(IV) to Sn(II) and then subsequently converted from Sn(II) to Sn(0). In contrast, we suggest that a semi-infinite diffusional process occurs within the thin-film-control electrode. This means the outer

portion of the film is converted to Sn(0) prior to the inner portion of the film. This

broadens the potential region over which the Sn(IV)-to-Sn(0) conversion occurs and

makes it impossible to see the individual component processes. This model is supported

by low scan-rate voltammograms obtained at the thin-film electrode (Figure 2-7), which

begin to show evidence for the two distinct reduction waves.

Constant Current Charge/Discharge Experiments

Constant current charge/discharge experiments were conducted in the potential

window between 0.2 V and 0.9 V. This narrow potential region was chosen because

Dahn's work has shown that better cyclability is obtained if both higher and lower

potential regions are avoided.[88,132] In agreement with the voltammetric results, the first

charge to 0.2 V shows a large irreversible capacity (total capacity for first charge = 3500

mAhg[-1]) associated with both the conversion of the Sn(IV) to Sn(0) and the formation of

the solid electrolyte interface (SEI) region at the electrode/solution interface.[133]
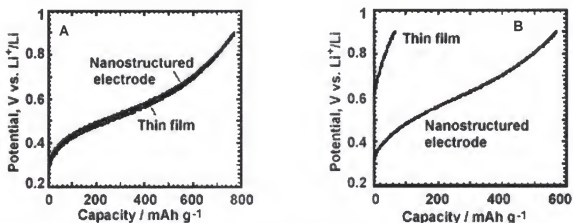
Figure 2-8. Discharge curves for the thin-film and nanostructured SnO_2 electrodes. At charge/discharge rates of A) 3 C and B) 32 C.

Figure 2-8 shows discharge curves for the nanostructured and thin-film electrodes

at discharge rates of 3 C and 32 C, respectively (1 C corresponds to a current density of

0.04 mA cm^{-2}). At the lower discharge rate, both electrodes show an experimental

capacity that is essentially identical to the theoretical capacity associated with Li alloying
of tin over this potential region (Figure 2-8A). As is always observed for Li-ion battery
electrodes, capacity falls off with increasing discharge rate.[59-61,130] However, the extent
of capacity loss is dramatically reduced for the nanostructured electrode (Figure 2-8B).
This is because in order to achieve full capacity, all of the Li$^+$ in the electrode must be
removed during discharge. As pointed out in our previous studies, this is more easily
accomplished when the distance over which Li$^+$ must diffuse in the solid state is
decreased, as it is in the nanostructured electrode. [59-61] This trend is clearly seen in Figure
2-9, which shows the discharge capacities of the nanostructured and the thin-film-control
electrodes as a function of discharge rate. At the highest rate, the nanostructured
electrode delivers two orders of magnitude greater capacity than the thin-film electrode.
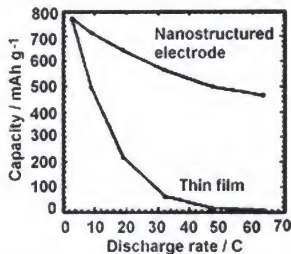
Figure 2-9. Discharge capacity *vs.* discharge C rate for the nanostructured and thin-film
SnO$_2$ electrodes.

Figure 2-10 shows the discharge capacity *vs.* the number of charge/discharge cycles
for the thin-film and the nanostructured electrodes. The capacity of the thin-film
electrode decreases with cycling, especially at the higher discharge rate of 8 C (Figure 2-
10A). In contrast, there is absolutely no loss of capacity with cycling for the

nanostructured electrode (Figure 2-10B) at either the high or low discharge rates. Indeed,

capacity initially increases with cycle number. To explore cycle life further, a

nanostructured electrode was cycled through 1400 cycles (Figure 2-11). In order to

decrease the timescale of this experiment, a very high charge/discharge rate (58 C) was

employed.
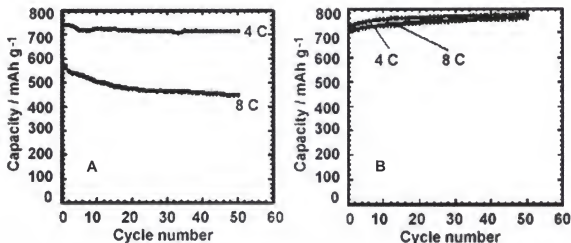
Figure 2-10. The relationship between the discharge capacity and cycle number. A) For the thin-film SnO_2 electrode. B) For the nanostructured SnO_2 electrode.
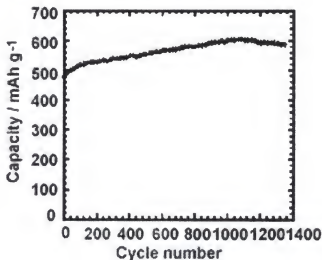
Figure 2-11. Cycle life of the nanostructured SnO_2 electrode over 1400 cycles at a charge/discharge rate of 58 C.

Again, capacity initially increases with cycle number; this trend is observed through the first 1000 cycles (Figure 2-11). That this increase in capacity is real is illustrated by the charge/discharge curves in Figure 2-12. The curves labeled a and a' are the charge and discharge curves for the first cycle, and the curves labeled b and b' are the corresponding curves for the 800th cycle. It is clear from these curves that both the charge and discharge capacities are greater after 800 cycles. This increase in capacity is caused by the increase in electrode surface area associated with the expansion of the fibers and with the formation of the bulbs at the ends of the fibers (Figure 2-4). The increase in electrode surface area with cycling means that the current density decreases with cycling. This allows for a greater amount of Li to be incorporated into the fibers before the potential cutoff is reached.
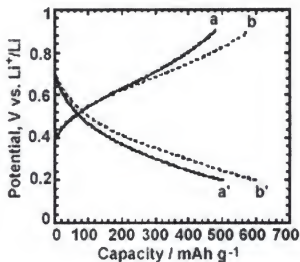
Figure 2-12. The charge and discharge curves for the nanostructured SnO_2 electrode.
A) For the first cycle (a and a'). B) For the 800th cycle (b and b').

The loss of capacity with cycling observed for conventional Sn-based anodes has been attributed to internal damage associated with the large volume changes that occur during lithium insertion and removal.[87,88] Apparently, the nanoparticles can relieve the

stress associated with these volume changes more easily. This is undoubtedly due to two causes. First, as discussed by Besenhard *et al.*,[87] in very small particles even large changes in the dimensions of the crystal structure due to incorporation of Li will result in small absolute changes in the dimensions of the particle. Second, because the nanoparticles are surrounded by electrolyte (and not by other particles) there is room for expansion of the particle. This is clearly seen by the bulb formation in Figure 2-4A. These bulbs can form without one fiber crushing its neighboring fibers.

Conclusions

The nanostructured Sn-based anodes prepared here show a combination of rate capability and cycle life far superior to any electrodes of this type described previously. Hence, this paper shows that combining basic research efforts in nanomaterials and Sn-based anodes could lead the way to the development of a new class of nanostructured anodes for Li-ion batteries. It is clear, however, that much additional research will be required before practical nanostructured anodes will be developed. Finally, it is of interest to note that another report on nanostructured Sn electrodes (prepared *via* a different route) has recently appeared; however, these electrodes showed poor cyclability and rate capabilities.[134]

CHAPTER 3
A NANOSTRUCTURED HONEYCOMB CARBON ANODE

Introduction

Carbonaceous anodes (e.g., graphite) are currently used in commercial Li-ion batteries,[135-137] and in agreement with our work,[59-61] Tran *et al.* and Zaghib *et al.* have shown that carbon anodes based on smaller sized particles have improved rate capabilities.[120,138] These results indicate that research on new types of nanostructured graphitic carbon might yield improved anode materials for Li-ion batteries. Masuda and co-workers have recently described an interesting nanostructured honeycomb diamond-like carbon material, and they have used this material to make a new class of electrochemical supercapacitors.[139] This honeycomb material consists of a thin diamond-like carbon film containing a highly ordered array of monodisperse nanoscopic pores that run through the thickness of the film. It occurred to us that a graphitic-carbon version of this honeycomb material might be an interesting new type of nanostructured carbon anode.

The honeycomb material was prepared by using a nanoporous alumina membrane as a mask to burn holes in an underlying diamond-like carbon film. We have used a modified form of this method to prepare honeycomb graphitic-carbon films that contain an array of 75 nm-diameter pores. When used as Li-insertion anodes, these honeycomb carbon films show dramatically improved rate capabilities relative to thin carbon films that do not contain the honeycomb of nanopores. The results of these investigations are described here.

Experimental

Materials

Aluminum foil (100 mm x 500 mm x 0.5 mm, purity 99.99%, Alfa Aesar), quartz slides (75 mm x 25 x 1 mm, ChemGlass), Li ribbon (1.5 mm thick, 100 mm wide, 99.9%, Aldrich), oxalic acid (Fisher), lithium perchlorate (99.99%, Aldrich), diethyl carbonate (99+%, Aldrich), ethylene carbonate (Aldrich) and Ethylene (30 % balanced with He, Praxair) were used as received.

Preparing the Nanoporous Alumina Membrane

We have used Masuda's two-step method for preparing high quality nanopore alumina membranes.[140] Briefly, the Al foil was first degreased using acetone and then annealed in air at 400 °C for 1 hour. A double-side 42 cm^2 section of foil was then electropolished at 15 V in a solution that was 95 wt.% H_3PO_4 + 5 wt.% H_2SO_4 and was 0.20 M in CrO_3. The cathode was a Pb plate. After rinsing with distilled water, the polished Al foil was anodized at 50 V in 5 wt.% aqueous oxalic acid at 1.5 °C for 1 hour. This time, the cathode was a stainless steel plate. This resulted in the formation of a thin nanopore alumina film on the surface of the Al foil. This precursor film was dissolved away in an aqueous solution that was 0.2 M in CrO_3 and 0.4 M in H_3PO_4 at 80 °C. As discussed by Masuda,[140] this leaves a highly ordered and textured pattern of scallops on the Al substrate.

In the second step, this textured Al substrate was anodized for 15 minutes at 50 V in the 5 wt.% aqueous oxalic acid solution. This yields the desired highly ordered nanopore alumina film. The voltage reduction technique was then used to detach this film from the underlying Al surface.[141] This entails gradually (over a period of 1 hour) reducing the anodizing voltage to 15 V, followed by detachment by immersion of the

surface in 10 wt.% H_3PO_4 solution. The resulting free-standing nanopore alumina membrane (1.2 µm thick) has two distinct surfaces – the barrier-layer surface, which faced the substrate Al foil during the anodization process, and the solution surface.

Preparing the Carbon Thin Films

The carbon films were prepared using a chemical vapor deposition (CVD) method described previously.[142] A quartz slide was inserted into the center of a quartz tube reactor housed in a high temperature tube furnace. The furnace was heated at 30 °C/min to 970 °C in flowing Ar gas. The flow rate of Ar is 90 standard cubic centimeters (sccm). The Ar gas stream was then replaced by ethylene (20.7 sccm), which decomposed on the quartz surface to yield the CVD graphitic carbon film.[142] After 2 hours of CVD reaction, the ethylene was replaced by Ar, and the furnace was allowed to cool to room temperature. This yielded carbon films that were 1 µm in thickness.

Preparing the Honeycomb Carbon Films

The nanoporous alumina membranes were used as masks, in conjunction with an O_2-plasma etching method, to prepare the honeycomb carbon films. First, however, the barrier-layer surface of the alumina membrane was etched in an Ar plasma to widen the pores at this surface. The alumina membrane was placed, barrier-layer surface up, on top of the CVD carbon film. This assembly was then inserted into the center of the vacuum chamber of a reactive ion etching system (Plasma-Therm 790 series), and an Ar plasma was used to etch the barrier-layer surface. This was accomplished using a plasma with radio frequency (rf) power of 200 W and inductively coupled plasma (ICP) power of 300 W. The plasma pressure was 2 mTorr Ar, the Ar flow rate was 15 sccm, and the etch time was 14 min.

After the Ar-plasma etching, the rf power was switched to 300 W, and the Ar was replaced by a mixture of O_2 (10 sccm) and Ar (5 sccm). The alumina-membrane/carbon-film assembly was exposed to this O_2 plasma for 2 minutes. During this time, the O_2 plasma propagated into the pores of the alumina membrane and etched away the portions of the underlying carbon film beneath the pores. This led to a honeycomb carbon film that is a replica of the pore structure in the alumina membrane mask (Figure 3-1).
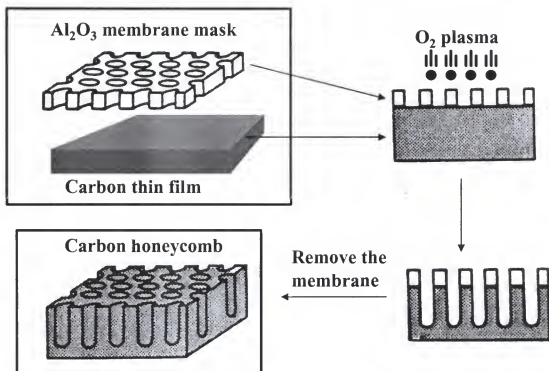
Figure 3-1. Schematic of honeycomb carbon preparation.

Preparing the Surface-Oxidized Carbon Thin Films

These films were prepared in order to explore the effect of surface oxidation on the Li^+ intercalation electrochemistry of the carbon films. A nonhoneycombed carbon film was placed in the center of the vacuum chamber of a bench-top plasma system (Micro-RIE Series 85, Technics International), and O_2 plasma etching was conducted for 1 minute (150 W, 300 mTorr O_2).

X-Ray Diffraction Experiments

X-ray diffraction studies were conducted on a MRD X'Pert X-ray diffraction system (Phillips) using Cu Kα radiation (weighted average wavelength $\lambda = 1.540560$ Å) in a glancing angle reflection mode. The data were collected between 10° and 80° 2Θ at a scanning step of 0.01° with a 1s interval between each step. Because the obtained X-ray diffraction pattern of the as-synthesized carbon film was overlapped by the diffraction peak from the quartz substrate, simulations were conducted by using the X'Pert organizer simulation software (Philips). Based on the simulation results, the background from the quartz substrate was subtracted out and the accurate diffraction data from carbon film was obtained.

X-Ray Photoelectron Spectroscopy (XPS) Analysis

XPS studies were performed on a Kratos XSAM 800 spectrometer with Mg Kα excitation (200 W). The samples were mounted onto a stainless steel sample stub by means of a 7 mm diameter carbon sheet disk (SPI supplies), so as to completely cover both the carbon disk and the sample stub. The samples were inserted into the sample analyzer chamber by means of a quick insertion probe, and spectral acquisition with the fixed analyzer transmission mode commenced after the pressure decreased to 5 x 10^{-9} Torr. Survey scans, high-resolution C 1s spectra was recorded at a takeoff angle of 45° relative to the sample surface. Data analysis was done by using the DS 800 software package. Peak positions were all referenced to 285.0 eV for the main carbon peak.

Scanning Electron Microscopy (SEM)

The sample was attached to an SEM sample stub using a piece of copper foil tape. To improve the quality of the SEM image, the surface of this sample assembly was then

sputtered with a very thin (<10 nm) Au film using a Hummer 6.2 (Anatech Ltd.)
sputtering system. Samples were imaged using a JEOL 6330 cold field emission
scanning electron microscope. For quantitative evaluations of the film thickness, pore
diameter, porosity, and pore-depth, data from three different SEM images were averaged.

Constant-Current Charge/Discharge Experiments

The Li^+ intercalation electrochemistry of three different carbon electrodes were
investigated. They include the as-synthesized (AS) CVD thin-film electrode, the AS
electrode whose surface had been O_2-plasma etched (this nonhoneycombed material is
designated as the PE electrode), and the honeycomb (HC) electrode. Electrochemical
experiments were run on an EG&G Princeton Applied Research Model 263
potentiostat/galvanostat in conjunction with a Gateway 2000 computer. A three-
electrode cell – AS, PE or HC working electrode and Li foils counter and reference
electrodes - was used. The electrolyte was 1 M $LiClO_4$ in a 30:70 (vol.%) mixture of
ethylene carbonate and diethyl carbonate. All electrochemical experiments were
conducted at room temperature in a glove box filled with argon. All potentials reported
in this paper are *vs* the Li^+/Li reference electrode. Constant-current experiments were
performed between 0 and 3 V (*vs.* Li^+/Li) at currents ranging from 10 to 600 μA. The
charge/discharge capacity was calculated from the charge/discharge times, the mass of
the carbon anode and the currents used.[60] The masses of the carbon electrodes were
obtained by measuring the mass difference between the bare quartz substrate and the
carbon-covered substrate. The balance used was a Mettler model AX205DR (accuracy $\pm$
0.01 mg).

Results and Discussion

Scanning Electron Microscopy

Figure 3-2A shows that the solution surface (*vide supra*) of the nanoporous alumina membrane has an array of pores that are on average of 66 nm in diameter with a porosity of 36.9%. In contrast, prior to Ar-plasma etching, it is difficult to see open pores on the barrier-layer surface (Figure 3-2B). The cross-sectional image (Figure 3-2C) shows that the barrier-layer surface is covered with a disordered matt of Al_2O_3, the remnants of the barrier layer that was present on this surface prior to voltage reduction and detachment.
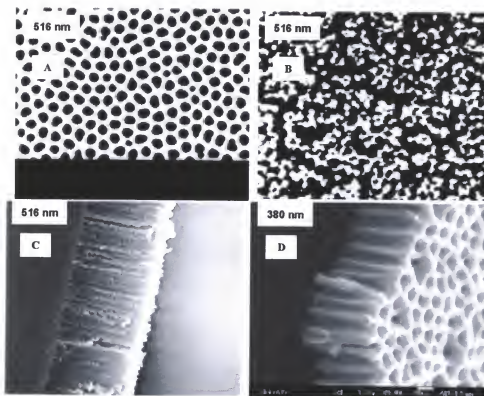
Figure 3-2.   Scanning electron micrographs of the nanoporous Al_2O_3 membrane. A) Solution surface. B) Barrier-layer surface. C) Cross section before Ar-plasma etching. D) Cross section after Ar-plasma etching.

Figure 3-2C also shows that the as-prepared membrane is 1.2 μm thick, and ~0.2 μm of this thickness is the barrier-layer matt. Figures 3-2D shows that Ar-plasma etching

removes the disordered matt from the barrier layer surface and opens the pores at this

surface. Ar-plasma etching also decreases the membranes thickness to 0.4 μm.
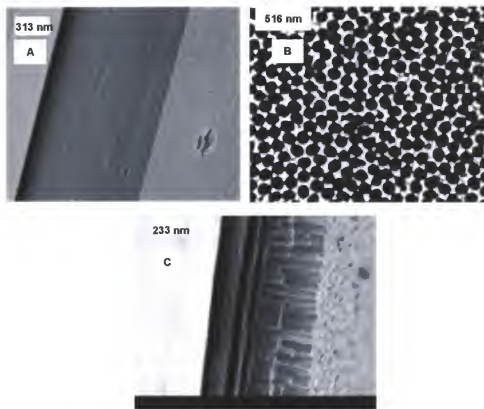
Figure 3-3. Scanning electron micrographs of different carbon films. A) Cross section of as-synthesized (AS) carbon thin-film. B) Surface and C) cross section of the honeycomb (HC) film.

Figure 3-3A shows a cross-sectional and surface image of an as-synthesized (AS)

CVD carbon film. Images of this type indicate that these films are defect-free and

spacing filling with smooth surfaces; the film thickness is 1μm. Figure 3-3B shows that

the surface of the honeycomb carbon (HC) film has a high density of monodisperse

pores with pore diameter ~75 nm, slightly larger than that of the alumina mask; the

porosity is 50%. The cross-sectional image (Figure 3-3C) shows that these pores do not

extend all the way through the thickness of the carbon film. Rather, the pore depth is

~420 nm and there is a base layer of unetched (nonporous) carbon that is ~370 nm thick.

This unetched portion of the carbon film allows for good electrical contact to the overlying etched portion of the film. The characteristics of the various carbon electrodes studied here are summarized in Table 3-1.

Table 3-1. Characteristics of the different carbon electrodes studied.

	Mass (mg)	Area (cm^2)	Pore diameter (nm)	Pore depth (nm)	Porosity (%)
As-synthesized (HC)	0.15	0.75			
O$_2$ plasma etched Surface(PE)	0.15	0.75			
Honeycomb(HC)	0.13	0.85	75	420	50
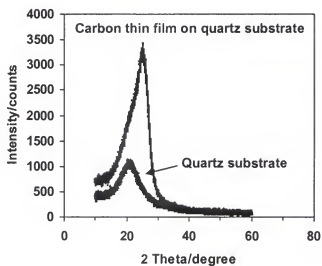
Figure 3-4. X-ray diffraction patterns for the quartz substrate and the as-synthesized carbon film on this substrate.

X-Ray Diffraction Experiments

Figure 3-4 shows X-ray diffraction data for the quartz substrate and for the AS carbon film on this substrate. The peak in the AS carbon-film data is due to the diffraction from d$_{002}$ plane, and the breadth of this peak shows that the film is disordered.[143,144] After correcting for the contribution from quartz we find that the d$_{002}$ peak of the carbon thin film occurs at lower angles than in graphite ($2\theta = 25.402^\circ$ *vs.*

$26.381°$ for graphite). Furthermore, the interlayer distance is expanded from 3.376 Å (graphite) to 3.497 Å. These features are typically of turbostratically-disordered carbon films prepared by the CVD method.[145]
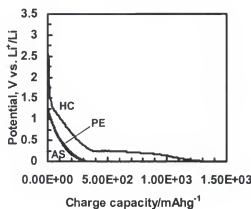
Figure 3-5. First constant-current charging curves for the honeycomb (HC), plasma-etched (PE), and as-synthesized (AS) electrode (at 0.2 C rate).
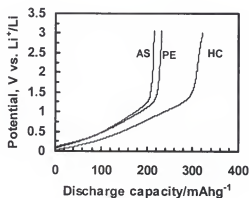
Figure 3-6. First constant-current discharging curves for the honeycomb (HC), plasma-etched (PE), and as-synthesized (AS) electrodes (at 0.2 C rate).

Constant Current Charge/Discharge Experiments

The AS, HC and PE electrodes were charged from the open circuit (~3 V) to 0 V (Figure 3-5). The charging curve for the HC film is distinctly different from those of the AS and PE films. In particular, much longer times are required before the potential of the

HC film reaches the negative limit of 0 V. The corresponding discharge curve (Figure 3-6) shows that a large portion of this first-charge capacity is irreversible. This indicates that the irreversible capacity of the HC electrode is larger than for either the AS or PE electrodes. Because the surface area of the HC electrode is much higher, this result is not surprising. We are currently studying the surface chemistry changes associated with this irreversible capacity, and we will report on these results soon.

Low-rate (0.2 C) discharge curves for the HC, AS and PE electrodes are shown in Figure 3-6. There are no potential plateaus, which corroborates the conclusion that these electrodes are composed of disordered carbon.[144] Gnanaraj *et al.* have explained that the small size of the elementary graphene flake fragments and the lack of long-rang order in the c lattice direction in disordered carbon preclude staging phenomenon during Li^+ insertion/extraction.[144] Figure 3-6 also shows that the reversible capacity of the HC electrode is significantly higher than the reversible capacities of the AS and PE electrodes. The reversible capacity of the HC electrode at this low discharge rate is almost 90% of the maximum theoretical capacity of graphite.
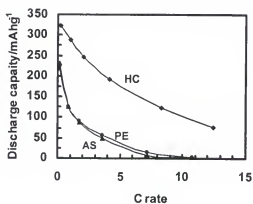
Figure 3-7. Discharge capacity *vs.* discharge C rate for the honeycomb (HC), plasma-etched (PE), and as-synthesized (AS) electrodes.

Figure 3-7 shows the discharge capacity *vs.* discharge rate data for the AS, PE and HC electrodes. As is typically observed for Li-ion battery electrodes, capacity falls off with increasing discharge rate.[59-61] As noted earlier, this is because the rate of discharge is limited by slow solid-state Li$^+$ diffusion in the electrode material.[59-61] The consequence of this slow Li$^+$ transport is that at high discharge rates, the surface of the electrode material becomes depleted in Li$^+$ causing the electrode potential to reach the positive cutoff value before Li$^+$ in the interior of the material can be deintercalated (i.e., concentration polarization).

In our previous papers we have shown that electrodes composed of monodisperse nanotubes and nanofibers of the electrode material are much less susceptible to the deleterious effects of concentration polarization than thin-film control electrodes composed of the same material.[59-61] This is because the distance Li$^+$ must be transported in the solid state is dramatically reduced in these nanostructured electrodes. As a result, the nanostructured electrode retains a much larger fraction of its theoretical capacity at high discharge rates than the corresponding thin-film control electrode.[59-61]
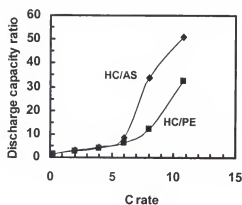
Figure 3-8. Ratio of the discharge capacitiy *vs.* discharge C rate for the honeycomb (HC), plasma-etched (PE), and as-synthesized (AS) electrodes.

Like the nanofiber and nanotube electrodes described previously, the HC electrode also shows dramatically higher discharge capacities at high C rates than the two thin-film electrodes (Figure 3-7). This shows, as might be expected, that the HC carbon is another form of nanostructured electrode. In this case, penetration of solvent and Li^+ electrolyte into the pore structure of the HC insures that the distance Li^+ must diffuse in the solid state is dramatically lower than in the AS or PE electrodes. This rate-capability advantage of the HC electrode can be shown more clearly by plotting the ratio of the discharge capacities of the HC and AS electrode *vs.* C rate (curve labeled HC/AS in Figure 3-8). At the highest C rate, the HC electrode delivers 50 times higher capacity than the AS electrode.

It is also of interest to compare the capacities of the HC *vs.* PE electrodes as a function of C rate (Figure 3-8). The HC electrode, again, shows better rate capabilities than the PE electrode, but the advantage is not as large as the HC *vs.* AS case. Put another way, the thin-film-control electrode whose surface had been O_2 plasma etched (PE) shows better rate capabilities than the non-plasma etched AS control electrode. There have been a number of recent studies of the effect of surface oxidation on the discharge properties of carbon electrode materials.[146,147] Peled *et al.* showed that mild oxidation (burning) of synthetic graphite resulted in electrodes that showed higher discharge capacities and longer cycle lives than the corresponding non-oxidized electrode.[146] Ein-Eli *et al.* chemically oxidized the surfaces of graphite electrodes and obtained similar benefits.[147] The key point to make here is that since the pores in the HC electrode are made by an oxygen-plasma method, the benefits of surface oxidation are inherent in the HC fabrication process.

X-Ray Photoelectron Spectroscopy Analysis

To further understand the influence of O_2 plasma etching on carbon thin film, XPS analysis was conducted and the results are shown in Table 3-2 and Table 3-3. Table 3-2 shows that no carboxylic group is detected on the surface of carbon thin film, but after oxygen plasma etching, almost 9% of the surface carbons are presented as carboxylic groups. Such result is compatible to those reported before.[146,147] By contrast, the percentage of C=O functional group is drastically reduced by oxygen plasma etching. Since C-O-C groups should be more stable against oxidation compared with C-OH groups, the 10.6% oxygenated C at 286.5 eV on the surface of oxidized carbon may be due to C-O-C group. In fact, a calculation of the changes at 286.5 eV and 288.8 eV gives:

$$(14.3\% - 10.6\%) + (6.6\% - 0.9\%) = 9.4\% \cong 8.8\%$$

Thus, one might postulate that oxygen plasma etching causes oxidation of C-OH and C=O functional groups to carboxylic groups.

Table 3-2. Binding energy and composition of the functional groups on the surface of the pure and the oxidized carbon thin-films before charge/discharge cycling.[148-150]

Assigned C 1s peak	Binding energy (eV)	Pure carbon	Oxidized carbon
Graphitic, C sp^2	284.1	59.3%	63.6%
C sp^3 and H terminated C	285.0	19.7%	16.1%
C-OH, C-O-C	286.5	14.3%	10.6%
C=O	288.8	6.6%	0.9%
O-C=O	289.0		8.8%

However, the composition of functional groups on the surface of the pure and the oxidized carbon thin films changed after the 1st charge/discharge cycling (Table 3-3). Table 3-3 shows that the first charge/discharge cycle causes a greater loss of graphitic carbon for the carbon thin-film than for the oxidized carbon. The loss in graphitic carbon

is almost balanced by the gain at 285.0 eV, which is where the amorphous carbon also shows up.[146] For the carbon thin-film we have: loss = 59.3% - 48.1% = 11.2% compared to gain = 33.9% - 19.7% = 14.2%. For the oxygen plasma etched carbon-thin film we have: loss = 63.6% - 57.5% = 6.1% compared to gain = 23.5% - 16.1% = 7.4%. It can be deduced that the solid electrolyte interface (SEI) film formed during the first charge on the surface of pure carbon thin film is less efficient than that on the surface of etched carbon thin-film.[133] As a result, co-intercalation of solvent molecules with Li^+ occurs. Therefore more ordered graphene planes are damaged for the pure carbon thin-film than for the etched carbon thin-film, leading to more amorphous carbon produced. In contrast, the carboxylic groups on the oxidized carbon thin film can be converted into Li-carboxylic salts during the first charge process to form chemically bonded SEI film. This dramatically increased the stability of the graphite anode, higher capacity and longer charge/discharge cycle life have been obtained in EC-DEC based electrolyte.[146,147]

Table 3-3. Binding energy and composition of the functional groups on the surface of the pure and the oxidized carbon thin-films after the first charge/discharge cycling. [148-160]

Assigned C 1s peak	Binding energy (eV)	Pure carbon	Oxidized carbon
Graphitic, C sp^2	284.1	48.1%	57.5%
C sp^3 and H terminated C	285.0	33.9%	23.5%
C-OH, C-O-C	286.5	11.4%	11.4%
C=O	288.8	6.6%	0.0%
O-C=O	289.0		7.6%
Carbonate	290.9	11.2%[a]	6.3%[a]

a. Out of total carbons on the surface

Figure 3-9 compares the cycle lives of the HC, PE and AS electrodes. In agreement with the above conclusions, the two O_2 plasma-etched electrodes (HC and PE) show better cycle life than the AS electrode. For example, the ratios of the capacities

obtained after the 50th cycle to that obtained for the first cycle for the HC, PE and AS
electrodes are 0.75, 0.77 and 0.53, respectively. Finally, Figure 3-10 shows that the HC
electrode delivers usable capacity even after 700 cycles.
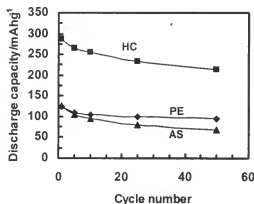
Figure 3-9.   Discharge capacity *vs.* cycle number for the honeycomb (HC), plasma-
etched (PE), and as-synthesized (AS) electrodes (charge/discharge rate = 1
C).
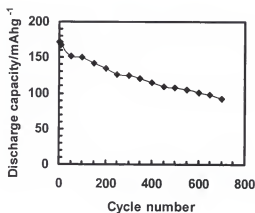
Figure 3-10.   Honeycomb-carbon electrode cycle life data for 700 cycles. For the first
50 cycles the charge/discharge rate was 1 C. For the remaining cycles the
charge/discharge rate was 2 C.

Conclusions

We have shown that a new type of nanostructured honeycomb carbon anode can be
prepared using an O_2 plasma etch method in conjunction with a nanoporous alumina
mask. These honeycomb carbon anodes show low-rate discharge capacities of 325 mA

hg^{-1}, and at high discharge rates (10 C), delivery 50-times the capacity of a thin-film-control anode that did not contain the honeycomb of nanopores.

CHAPTER 4
INVESTIGATING A NANOSTRUCTURED SOLID-STATE LI-ION BATTERY

Introduction

As noted above, Li-ion batteries are compact and lightweight with very high-energy density (Table1-1). They are becoming the most suitable power sources for aerospace, modern health care and portable consumer electronics applications.[151-153] However, Li-ion batteries are facing two shortcomings. First, due to the slow diffusion of Li^+ in solid-state electrodes (diffusion coefficient $\sim 10^{-9} - 10^{-11}$ cm^2s^{-1} in carbon,[154,155] SnO_2,[156] $LiMn_2O_4$,[157] $LiCoO_2$,[158] and V_2O_5,[159]), the rate capability of Li-ion batteries is low. That means it can not deliver a high capacity at a high discharge rate, second, the nonaqueous electrolyte used should be handled in an inert gas-protected glove box or an environment with ppm contents of H_2O and O_2. It is very inconvenient in handling, fabrication and shipping.

In order to overcome the first shortcoming of Li-ion batteries, we have been exploring the use of a template-synthesis method to prepare nanomaterials, which can be used as electrodes of Li-ion batteries. In Chapter 2, it has been demonstrated that these nanostructured Li-ion battery electrodes showed better rate capabilities than conventional electrodes composed of the same materials. Better rate capabilities are obtained because the distance over which Li^+ must diffuse in the solid state is dramatically decreased in the nanostructured electrode. Furthermore, the surface area of the nanostructured electrode is larger, making the effective current density during discharge smaller than for a conventional electrode discharged at the same current density.

Now the question is how we can overcome the problem of the inconvenient handling of the nonaqueous electrolyte of Li-ion battery. One of the promising efforts is to make an all-solid-state thin-film Li-ion battery, where the electrolyte is a solid material as well.[160-165] These batteries have potential applications as power sources of microelectronics including implantable medical devices, remote sensors, miniature transmitters, smart cards, and micro-electro-mechanical system (MEM) devices.[160-165] Solid electrolytes have several potential advantages over liquid electrolytes, such as no leakage problem, broad operating temperature range, excellent charge-discharge cyclic properties due to a lack of side reactions occurring, and long life because of little self-discharge. The most widely used solid electrolytes are based on inorganic lithium phosphorus oxynitride,[166] or organic polymers such as poly(ethylene oxide) and poly(acrylonitrile).[167] Due to the limitations in the preparative methods, their thickness should be more than 1 μm.[166-167]

In our research group, we have been exploring the possibility of combining the advantages of nanostructured electrodes and solid electrolyte to make a nanostructured all-solid-state Li-ion battery. In this approach, the carbon honeycomb discussed in Chapter 3 is used as both the anode and the substrate; solid electrolyte and cathode material are then deposited into it to make an all-solid-state nanostructured Li-ion battery. This concept is illustrated in Figure 4-1. However because the pore diameter of the carbon honeycomb is only 75 nm, conventional solid electrolytes can not be used (thickness > 1μm, as mentioned above). To solve this problem, our strategy here is to electropolymerize ultrathin poly(phenylene oxide) (PPO) films within the pores of the anode. The PPO is then sulfonated to make it cation conductive. The PPO was chosns

because it has been shown that ultrathin (5-7 nm) defect-free films of PPO can be obtained by a simple electropolymerization method.[168] The electropolymerized PPO films are demonstrated and discussed in this chapter.
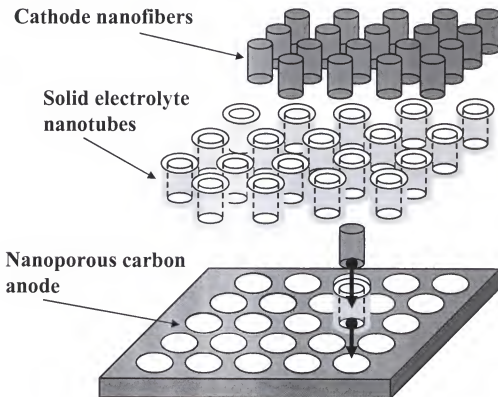
Figure 4-1. Schematic of the design of the nanostructured Li-ion battery.

Experimental

Materials

Phenol (99+%, Aldrich), tetramethylammonium hydroxide (97%, Aldrich) ($Me_4N^+OH^-$), tetrabutylammonium perchlorate (Aldrich) (Bu_4NClO_4), Potassium ferricyanide(III) (99+%, Aldrich), hexaamineruthenium(III) chloride (Aldrich), acetonitrile (Aldrich) (CH_3CN), methanol (Aldrich), Sulfuric acid (fuming, Aldrich) were used as received.

Cyclic Voltammetric Experiments

Cyclic voltammetric experiments were performed in a typical 3-electrode cell using a Solartron 1287 electrochemical interface module (Solartron Analytical, Hampshire, England) connected to a Solartron 1255B frequency response analyzer and a personal computer. The reference electrode was Ag/AgCl reference electrode, and the counter electrode was Pt foil. The geometric area of the working electrode was ~ 0.9 cm^2. Both the carbon thin-film and the carbon honeycomb (that were prepared by methods mentioned in Chapter 3) were used as working electrodes.

Electropolymerization of Phenol

The phenol monomer solution was 0.05 M tetramethylammonium hydroxide plus 0.05 M Phenol and 0.1 M tetrabutylammonium perchlorate. The solvent was acetonitrile. The electropolymerization was performed using the cyclic voltammetry method. The potential was first scanned from the open-circuit potential of ~ 0 V to the higher (positive) limit of 0.9 V; then the potential was scanned back to the lower (negative) limit of -0.45 V. The next two cycles were scanned between – 0.45 V and 0.9 V, and the final potential is at 0 V. The scan rate used was 10 mV s^{-1}. After electropolymerization, the working electrode was rinsed with acetonitrile several times before use.

Electrochemical Evaluation of the Poly(phenylene oxide) Thin Films

The PPO films were investigated using redox-active Fe(CN)$_6$$^{3-}$ and Ru(NH$_3$)$_6$$^{3+}$ ions. In this approach, cyclic voltammetry was conducted for both ions at a scan rate of 20 mV s^{-1}. When Fe(CN)$_6$$^{3-}$ ion was used, the first scan was started at the open-circuit potential of ~ 0.4V, and then the potential was scanned to the lower (negative) limit of 0.1 V. The return (positive-going) scan was then reversed to the higher (positive) potential of 0.52 V. The next two cycles were scanned between 0.1 V and 0.52 V, and

the final potential was at 0.4 V. The solution used was 12 mM $K_3 Fe(CN)_6$ plus 3 M

NaCl. When $Ru(NH_3)_6^{3+}$ ion was used, the first scan was started at the open-circuit

potential of ~ 0 V, and then the potential was scanned to the lower (negative) limit of -

0.4 V. The return (positive-going) scan was then reversed to the higher (positive)

potential of 0.05 V. The next two cycles were scanned between - 0.4 V and 0.05 V, and

the final potential was at 0 V. The solution used was 12 mM $Ru(NH_3)_6Cl_3$ plus 3 M

NaCl.

Sulfonation of the Poly(phenylene oxide) Thin Films Obtained

The sulfonation of PPO was simply performed by using a dipping method. In brief,

the electrode (carbon thin-film) was first electropolymerized with PPO; second, this

electrode was rinsed for several times with acetonitrile; third, the PPO covered electrode

was immersed into a instantly prepared solution of methanol plus fuming sulfuric acid

(1:1.5 vol.) for 10 s, then it was immediately removed from the solution and rinsed with

distilled water.

Scanning Electron Microscopy and Contact Angle Measurements

Samples were imaged using a field-emission scanning electron microscope (Hitachi

S-4000). The sample was attached to a SEM sample stub using a piece of conductive

copper foil tape. To improve the quality of the SEM image, the surface of the sample

assembly was sputtered with a thin (~ 10 nm) Au-Pd film using (Denton Vacuum, Desk

II sputter/etch unit). Water-drop contact angel measurements were conducted using a

Tantec contact angle meter.

X-Ray Photoelectron Spectroscopy Analysis

XPS studies were performed on a Kratos XSAM 800 spectrometer with Mg Kα

excitation (200 W). The samples were mounted onto a stainless steel sample stub by

means of a 7 mm diameter carbon sheet disk (SPI supplies), so as to completely cover

both the carbon disk and the sample stub. The samples were inserted into the sample

analyzer chamber by means of a quick insertion probe, and spectral acquisition with the

fixed analyzer transmission mode commenced after the pressure decreased to 5×10^{-9}

Torr. Survey scans, high-resolution C 1s spectra was recorded at a takeoff angle of 60º

relative to the sample surface. Data analysis was done by using the DS 800 software

package. Peak positions were all referenced to 285.0 eV for the main carbon peak.

Results and Discussion

| Phenol | Phenolate | Phenol radical |
| OH | O $^-$ | O $\bullet$ |

Figure 4-2.   Schematic of the anodic oxidation of phenol.

Electropolymerization of Phenol

The electropolymerization of tetramethylammonium phenoxide from acetontrile on

Pt or Au electrodes to prepare passive, ultrathin dielectric films of poly(phenylene oxide),

PPO, was first reported by McCarley et al.[168] Their study showed that PPO films could

have exceptionally low permeabilities to solution redox species, depending on

electropolymerization potential, the time of deposition, and the cross-linking reactions.

The prepared PPO films blocked the cyclic voltammetry of ferrocene carboxylic acid and

Cl⁻ oxidations in acetonitrile by > 99% and 92%, respectively, and reduction of

$Fe(CN)_6{}^{3-}$ and oxidation of the sodium salt of ferrocene carboxylic acid in water by $\geq$

99%. The thickness of the obtained PPO based on profilometry, ellipsometry, XPS and

high frequency electrical capacitance measurements was 5 - 7 nm. The electropolymerization of phenol is a radical initiated polymerization, and the radical is generated through anodic oxidation.[169] The anodic oxidation process is shown in Figure 4-2. In this process, phenol is first reacting with tetramethylammonium hydroxide to form tetramethylammonium phenoxide (phenolate); second, the phenolate is anodically oxidized into phenol radical, which is the initiator of phenol polymerization.

Potential / V vs. Ag/AgCl

Figure 4-3. The first three cyclic voltammograms for the electropolymerization of phenol.

To explore the electropolymerization conditions, the carbon thin-film electrode (discussed in Chapter 3) rather than the carbon honeycomb was first used. The electropolymerization was conducted by cyclic-voltammetrically scanned the carbon thin film electrode in the phenol monomer solution for 3 times in the potential window between – 0.4 V and 0.9 V (Figure 4-3). During the first positive scan, a huge oxidation peak appears at 0.25 V, indicating the anodic oxidation of phenol. Following the first

cycling, there is no oxidation peak, indicating the ending of phenol oxidation. Because

the anodic oxidation of phenol happens around 0.2 V, this means that the potential

window (-0.45 to 0.9 V) used here is suitable for complete phenol electropolymerization.

Figure 4-4. Scanning electron micrographs of the carbon thin-film electrode. A) Before
electropolymerization of Phenol. B) After electropolymerization of Phenol.
C) After sulfonation of PPO.

Scanning Electron Microscopy (SEM)

The SEM images of the carbon thin-film before and after electropolymerization,

and after PPO sulfonation are shown in Figure 4-4. Figure 4-4A shows that before

electropolymeization of phenol, the surface of the carbon thin film is a little rough.

However after PPO deposition on the carbon thin film (Figure 4-4B), the surface

roughness of the carbon thin film is decreased, indicating the deposition of PPO. Figure

4-4C shows that the surface roughness is increased after sulfonation. One possible reason

for the increase in surface roughness is that part of PPO film has been removed by

sulfuric acid.

Table 4-1. Binding energy and composition of the functional groups on the surface of
PPO free, PPO coated and PPO sulfonated carbon thin-films [148-150]

Assigned C 1s peak	Binding energy (eV)	Carbon	Carbon coated with PPO	Carbon coated with Sulfonated PPO
Graphitic, C sp^2	284.1	57%	24%	42%
C sp^3 and H terminated C	285.0	24%	50%	34%
C-OH, C-O-C	286.5	12%	19%	17%
C=O	288.8	7%	7%	7%

X-Ray Photoelectron Spectroscopy Analysis

XPS is a good analytical technique to study the surface chemistry of carbon by

means of the binding energies of C1s. After XPS measurements, curve fitting was

performed with the use of a standard least-square algorithm. The fitting results can

provide the atom percentages of different carbon-containing species on the surface.

Based on the XPS measurements and curve fitting results, the binding energies and the

composition of functional groups on the surface of carbon thin-films before and after

PPO deposition, and after PPO sulfonation were obtained. These data are shown in Table

4-1.

Table 4-1 shows that after PPO deposition, the amount of sp^3 carbon and

hydrocarbon on the carbon thin-film is dramatically increased, at the same time the

amount of graphitic carbon is decreased. These changes reflect the truth that the carbon

thin film has now been covered by PPO polymer film, which blocks and reduces the

intensity of graphitic carbon from the original carbon thin-film. The intensity of sp^3 is

increased because after PPO deposition, more sp^3 carbon is brought in by PPO polymer.

In Table 4-1, it also shows that the deposition of PPO on the carbon thin-film results in the increase in the amount of C-OH and C-O-C carbons. This increase could come from the PPO polymer film that has C-O-C groups. It should be noted that the amount of C=O carbon remains unchanged before and after PPO deposition. This happens because first, the PPO polymer includes no C=O group; second, the PPO film is so thin that the intensity of C=O from the underlying carbon thin-film could not be blocked.

Comparing the XPS data of PPO before and after sulfonation, it could be found that after sulfonation, the amounts of sp^3 carbon, C-OH and C-O-C carbons are decreased; the amount of graphitic carbon is increased; and the amount of C=O carbon remains unchanged. These results indicate that part of PPO film has been removed after sulfonation, and the intensity of graphitic carbon from the original carbon thin-film is restored.

It was diffcult to measure the thickness of the PPO film, which is so thin that conventional thickness-measurement techniques can not be used here. To solve this problem, an indirect method was used in this study. In this approach, we assume that the XPS spectra peak of graphitic carbon is due solely to the original carbon thin-film. Since the XPS data for PPO free as well as PPO coated carbon thin-films at the same angle of observation were obtained here, the thickness (t) of PPO film can be estimated using the practical effective attenuation length L, for the graphitic C 1s peak. The relationship between L and t is given in Equation 4-1[170]

$$L = [1/\cos \theta][t / \ln(I_0/I)] \qquad (4\text{-}1)$$

where θ (30° in this study) is the takeoff angle that is relative to the surface normal for the emitted electrons; I_0 and I are the integrated areas of graphitic carbon for the PPO free

and PPO coated carbon thin-films, respectively; A value of L = 23.3 Å is calculated based on the published data. [170] The density of carbon thin-film is taken to be the same as the density of graphite. Solving Equation 4-1 by using the obtained XPS data gives t = 1.9 nm (before sulfonation) and 0.5 nm (after sulfonation). This again confirms that the thickness of PPO is decreased after sulfonation.

XPS may also help us to indirectly detect the existence of PPO film on the carbon thin-film. Table 4-1 shows that for the carbon thin-film without PPO coating, the composition ratios of the graphitic carbon to sp^3, and C-OH and C-O-C carbons are 57:24 and 57:12, respectively. If we could assume this ratio has no change after PPO coating (in the case that the contamination from PPO can be negligible), then, according to the composition of graphitic carbon (24%) on the PPO coated carbon thin-film, the compositions of sp^3 and C-OH and C-O-C carbons from the underlying carbon thin-film can be 10% and 5% respectively. That means by subtracting these underlying carbon thin-film related C 1s compositions from those of the totally obtained C 1s compositions, the PPO-related compositions of sp^3 carbon (50% -10% = 40%), and C-OH and C-O-C carbons (19% - 5% = 14%) can be obtained. This gives a ratio (sp^3 carbon to C-OH and C-O-C carbons for PPO film) of 40/14 =2.9, which is in excellent agreement with the expected ration of 3.0 for PPO film.

Cyclic Voltammetric Experiments

Redox-active ions are used in this study to investigate the obtained PPO films. These ions were chosen because the cyclic voltammograms of them could give you a quick and direct indication about the quality of the prepared PPO films. The following strategy was taken; before PPO deposition, the ions are reactive on the electrode (e. g. carbon thin-film); after PPO deposition, the ions are not reactive because the PPO is

defect free and impermeable to ions; after PPO sulfonation, due to the existence of

negatively charged SO_3^- groups and electrical attraction, the redox-active cation can come

across the membrane to reach the electrode surface and to be reactive again; at the same

time the redox-active anion remains unreactive due to the electrical repulsion. Because

Li^+ is a cation, the cation-conductive PPO films could be used as electrolyte material for

Li^+ transport. The redox-active ions used here are positively charged $Ru(NH_3)_6^{3+}$ and

negatively charged $Fe(CN)_6^{3-}$. Their redox reactions are show in Equations 4-2 and 4-3.

$$Ru(NH3)_6^{3+} + e^- \xrightleftharpoons[\text{oxidation}]{\text{reduction}} Ru(NH_3)_6^{2+} \qquad (4\text{-}2)$$

$$Fe(CN)_6^{3-} + e^- \xrightleftharpoons[\text{oxidation}]{\text{reduction}} Fe(CN)_6^{4-} \qquad (4\text{-}3)$$
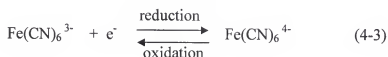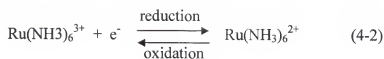
Figure 4-5 shows the first three cyclic voltammograms of $Fe(CN)_6^{3-}$ ion on the

PPO free, PPO coated and PPO sulfonated carbon thin-film electrodes. It can be found

that $Fe(CN)_6^{3-}$ ion is reactive on the PPO-free carbon thin-film electrode, because

apparent reduction and oxidation peaks are found at ~ 0.23 V and ~ 0.36 V, respectively.

However these peaks disappear on the PPO-coated carbon thin-film electrode, indicating

that the deposited PPO film is impermeable for $Fe(CN)_6^{3-}$ ion. In this situation, it is hard

to say the PPO film is defect free, because a very small reduction current can be found at

0.1 V, which could be caused by water reduction. Figure 4-5 also shows that, after PPO

sulfonation, there are still no reduction and oxidation peaks at ~ 0.23 V and ~ 0.36 V,

indicating $Fe(CN)_6^{3-}$ ion can not come across the sulfonated PPO film. Compared with

the cyclic voltammograms before sulfonation, it can be found that the reduction current

from the pin holes of the PPO film is increased. This pin-hole current increase could be

due to the PPO film thinning as indicated from the XPS data, or due to enlargement of

pin holes.

Potential/V vs. Ag/AgCl
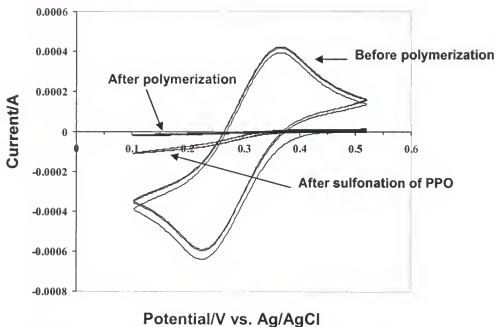
Figure 4-5. The first three cyclic voltammograms for the carbon thin-film electrode in
12 mM $K_3Fe(CN)_6$ + 3 M NaCl solution

Figure 4-6 shows the cyclic voltammograms of $Ru(NH_3)_6^{3+}$ ion on PPO free, PPO

coated and PPO sulfonated carbon thin-film electrodes. There are apparent reduction and

oxidation peaks on the PPO-free carbon thin-film electrode. The reduction peak is

located at ~ -0.26 V and the oxidation peak is located at ~-0.14 V. We can find that the

redox peaks of $Ru(NH_3)_6^{3+}$ disappear on the PPO-coated carbon thin-film, indicating the

PPO film is impermeable to $Ru(NH_3)_6^{3+}$ ion. However, after sulfonation of PPO, the

reactivity of $Ru(NH_3)_6^{3+}$ ion is resumed. This is possibly because there is electrical

attraction between the negatively charged carbon thin-film surface and the positively

charged $Ru(NH_3)_6^{3+}$ ion, and such an attraction enhances the transport of $Ru(NH_3)_6^{3+}$ ion

through the PPO film to reach the carbon thin-film surface.
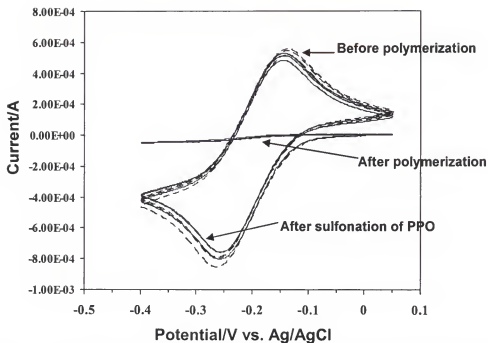
Figure 4-6.   The first three cyclic voltammograms for the carbon thin-film electrode in 12 mM $Ru(NH_3)_6Cl_3$ + 3M NaCl solution

Figure 4-5 and 4-6 show that the sulfonated PPO film is a conductor for cations, which means that this type of film can be used as solid electrolyte material for Li^+ transport in an all-solid-state Li-ion battery. Now the question is whether or not we can deposit PPO inside the nanopores of carbon honeycomb with a pore diameter of 75 nm. Figure 4-7 shows the SEM images of carbon honeycomb before and after PPO deposition. There is no apparent difference between the PPO coated and PPO free carbon honeycombs, indicating that the deposited PPO film can not block the nanopores of the carbon honeycomb.

Based on the experimental results above, we can find carbon honeycomb and sulfonated PPO thin film are suitable to be used as the anode and the solid electrolyte for a nanostructured Li-ion battery. The next step of our research is to deposit cathode

nanofibers inside the PPO nanotubes. The cathode material could be V_2O_5 that could be easily prepared through a so-gel method
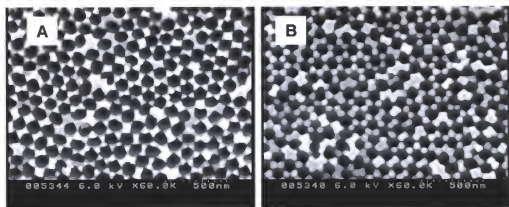
Figure 4-7. Scanning electron micrographs of the carbon honeycomb electrode. A) before and B) after electropolymerization.

Conclusions

A nanostructured all-solid state Li-ion battery can be prepared using the carbon honeycomb as the anode, sulfonated PPO thin film as the solid electrolyte, and V_2O_5 as the cathode. The research conducted here was focused on the preparation and the characterization of the PPO thin film. Cyclic voltammetric and SEM experimental results show that sulfonated PPO thin film is a good conductor for cations but an insulator for anions. Because PPO film is very thin (0.5 – 1.9 nm), it is a very suitable to be used as the solid electrolyte material for the nanostructured Li-ion battery.

CONICAL-NANOPORE MEMBRANES – PREPARATION AND TRANSPORT
PROPERTIES

Introduction

We have been investigating applications of nanopore membranes in analytical

chemistry – specifically in membrane-based bioseparations,[25,27, 118,119] electroanalytical

chemistry,[77,171,172] and in the development of new approaches to biosensor design.[105,173]

While the membranes that we typically use contain cylindrical nanopores, conically

shaped pores may offer some advantages for these analytical applications. For example,

in membrane-based bioseparations it is essential to maximize permeate flux through the

membrane. As we will show here, membranes with conical pores can have dramatically

higher rates of transport than analogous cylindrical-pore membranes. In addition, we are

interested in developing abiotic equivalents of protein-channel based stochastic

biosensors,[105] and conical pores would prove very useful for this application as well.

For these reasons, we needed to develop a simple method for making conical-

nanopore membranes. One approach we are exploring builds on the work of Apel *et al.*

who have shown that conical nanopores can be chemically etched into radiation-tracked

polymeric films.[174] We are also investigating a simpler alternative method, which is

based on O_2-plasma etching the surface of a track-etched (*vide infra*) polymeric film. We

have found that this plasma-etch method allows for control over the shape of the resulting

nanopores. For example, the plasma-etched pores may be cylindrical through most of the

membrane thickness blossoming into cones at one face of the membrane (trumpet-

shaped) or they may be nearly perfect cones. We have used measurements of membrane ionic resistance to demonstrate the enhanced transport properties of these conical pore membranes. The results of these investigations are described here.

Experimental

Membranes

Because the membranes investigated here are prepared by the track-etch method, we first briefly review this process. The track-etch method entails bombarding a solid material with a collimated beam of high-energy nuclear fission fragments to create parallel damage tracks in the film.[66] The damage tracks are then chemically etched into monodisperse cylindrical pores by exposing the tracked film to, for example, a solution of aqueous base. The diameter of the pores obtained is determined by the etch time and the etch-solution temperature. The pore density (pores per cm^2 of membrane area) is determined by the exposure time to the fission-fragment beam. Filtration membranes of this type having cylindrical pores with diameters ranging from as small as 10 nm to as large as 20 μm, and pore densities as high as 6 x 10^8 cm^{-2}, are sold commercially.

The membranes used here were 5.9 μm-thick polycarbonate films obtained by special order from Osmonics (Bryan, TX). The as-received membranes were tracked but not yet etched, and had a track density of 7 x 10^4 cm^{-2}. Track density was determined by etching the tracks into pores and taking low magnification field emission scanning electron microscopic images of the membrane surface. Data from nine different images were averaged.

Pore Etching

Conically shaped nanopores were produced by first chemically etching and then plasma etching the as-received tracked membrane (Figure 5-1). Chemical etching was

done at room temperature (23 °C) by simply immersing a sample of the tracked membrane (area ~25 cm^2) into a glass beaker filled with 100 ml of 6 M NaOH solution (Figure 5-1A). The membranes were immersed in this chemical etch solution for 12 min and then immersed for 1 h in 1 M formic acid to neutralize the base in the pores. The membrane was then immersed for 1 h in purified water at 40 °C, rinsed with purified water, and stored in air. As indicated in Figure 5-1B, chemical etching yields cylindrical pores.
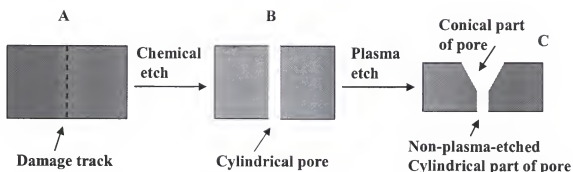
Figure 5-1.   Schematic of the plasma-etch process

Conically shaped pores were obtained by O$_2$-plasma etching one face of the cylindrical-pore membrane (the upper face in Figure 5-1C). A 1.6 cm x 1.6 cm piece of the cylindrical-pore membrane was placed on an 8 cm x 5 cm glass slide (1 mm thick). As discussed previously,[175] one surface of these membranes appears shinny the opposite surface appears rough to the eye. The membrane was placed on the glass slide with the shinny surface up. A 4 cm x 2.5 cm glass slide that had a 1 cm x 1 cm hole cut through it was placed on top of the membrane, and Scotch tape was use to attach the upper and lower glass slides. The tape did not cover the hole through the upper slide, and this hole defined the area of the membrane exposed to the O$_2$ plasma.

Plasma etching was done with a commercial reactive ion etch system (Samco, model RIE-1C). The etching conditions were as follows: O_2 gas pressure = 300 Pa, gas flow rate = 30 standard cm^3 min^{-1}, and power = 100 W. As indicated in Figure 5-1C, plasma etching enlarges the pore diameter at the upper surface, but the pore diameter remains unchanged at the lower surface. Furthermore, plasma etching thins the membrane (Figure 5-1C).

Membrane Burst Strength

A simple burst test was used to explore the effect of the plasma-induced thinning (Figure 5-1C) on the mechanical properties of the membrane. A circular sample of the membrane (diameter = 6.5 mm) was mounted between the two halves of a U-tube permeation cell.[119] The feed half-cell was pressurized with Ar gas, while the permeate half-cell was left open to air. The Ar gas pressure was increased until the membrane burst, and the pressure required to burst the membrane was recorded.

Scanning Electron Microscopy (SEM) and Contact Angle Measurements

Samples were imaged using an Hitachi S-4000 field-emission electron microscope. The membrane sample was attached to a SEM sample stub using a piece of conductive copper foil tape. To improve the quality of the SEM image, the surface of the sample assembly was sputtered with a thin (~10 nm) Au-Pd film using a Denton Vacuum, Desk II sputter/etch unit. To obtain quantitative values for the pore diameter and membrane thickness, data from three different images were averaged. It has been shown previously that plasma etching the surfaces of track-etched membranes enhances hydrophilicity.[176] To explore this issue we measured water-droplet contact angles using a Tantec contact-angle measuring system.

Electroless Plating of Conical Au Nanostructures within the Pores

A convenient way to investigate the shape of the pores in a track-etched membrane is to plate gold within the pores, remove the polymeric membrane material, and then obtain electron micrographs of the exposed Au nanostructures (Figure 5-2).[177] The nanostructure provides a negative image of the pore. An electroless plating method was used to deposit the Au nanostructures within the pores.[81] This method yields the conical Au nanostructures within the pores as well as Au surface films coating both faces of the membrane (Figure 5-2A).
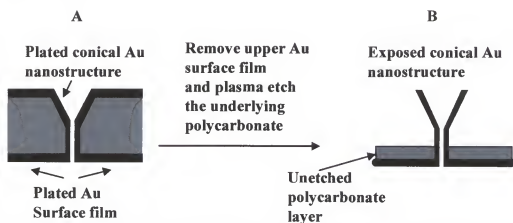
Figure 5-2. Schematic of the gold nanostructure-based method used to image the conical pores

A plasma etch method, described previoulsy[177], was then used to remove the polycarbonate membrane and expose the Au nanostructures plated within the pores. As illustrated in Figure 5-2B, the plasma etch process was terminated before all of the polycarbonate was removed. The remaining thin (<1 μm) polycarbonate film acts as a base to hold the exposed Au nanostructures in place. Finally, while Figure 5-2B shows an exposed conical Au nanostructure with the base of the cone facing up, samples with the tips facing up were also prepared.

Alternative-Current (AC) Impedance Measurements

AC impedance was used to explore the effect of conical pore formation (and membrane thinning) on the transport properties of the membrane. The membrane was mounted between the two halves of a U-tube cell, and both half-cells were filled with 4.5 mL of 3 M NaCl. A Pt wire working electrode was immersed into one half-cell solution, and a Pt wire counter electrode, and a Ag/AgCl reference electrode, were placed in the other half-cell solution. Impedance data were obtained using a Solartron 1287 electrochemical interface module connected to a Solartron 1255B frequency response analyzer and a personal computer. The magnitude of the sinusoidal potential perturbation applied across the membrane was $\pm$ 20 mV. Impedance data were obtained over the frequency range 10^6 Hz to 1 Hz. Z-plot and Z-view software packages (Scribner Associates, Inc.) were used to control the experiments and analyze the impedance data.

Commercially available track-etched polycarbonate membranes are typically treated with poly(vinylpyrrolidone) (PVP) to improve pore wetting. We encountered considerable difficulty in wetting the cylindrical pores obtained from the chemical-etch procedure. For this reason, prior to impedance measurements, all membranes were sonicated in 15 wt.% aqueous PVP and then rinsed with ethanol.

Results and Discussion

Scanning Electron Microscopic Images Showing Conical Pore Formation

Figure 5-3A shows an SEM image of the shinny surface of a chemically etched (but not O_2 plasma-etched) membrane. Only one pore is seen in this image because of the low pore density. Images of this type yielded a pore diameter for the chemically-etched membrane of 58 $\pm$ 6 nm, and analogous images of the opposite (rough) surface of the membrane gave the same pore diameter.

Figure 5-3B shows an image of the surface of a membrane that had been chemically etched to yield the cylindrical pores and then subsequently O_2-plasma etched for 5 min. The pore diameter at this membrane surface has been increased to 655 nm by the plasma-etch process. Images of the opposite face of the membrane (down during plasma etching) showed that the pore diameter was still 58 nm. This indicates that the plasma does not propagate down the entire length of the pore and that, as per Figure 5-1C, the pore in the upper portion of the membrane is now conically shaped.
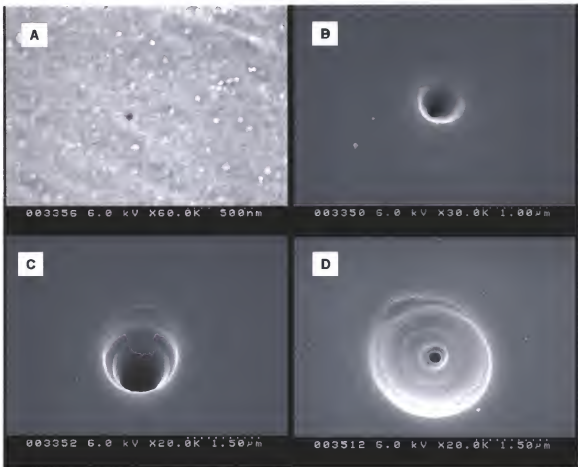
Figure 5-3. Surface scanning electron micrographs of the membranes after chemical and plasma etching. A) After chemical etching, and after B) 5 minutes, C) 10 minutes and D) 20 minutes of plasma etching.

Figures 5-3C and 5-3D show analogous images for membranes that had been chemically etched to yield the cylindrical pore and then O_2 plasma etched for 10 min and

20 min, respectively. We see that the pore diameter at the plasma-etched surface

increases with etch time (Figure 5-4). Images of the opposite membrane surface showed

a pore diameter of 58 nm, indicating, again, no plasma etching at the lower surface of the

membrane. These data show that the cone angle of the conical part of the pore increases

with plasma-etch time.
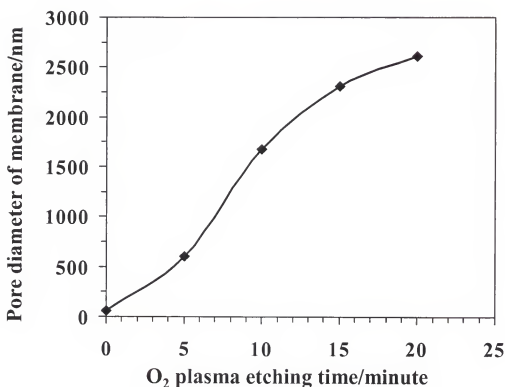
Figure 5-4. Plot of the pore diameter at the plasma-etched face *vs.* plasma-etch time.

Using Plated Au Nanostructures to Explore Pore Shape

As illustrated in Figure 5-2B, if a membrane is chemically etched but not

subsequently plasma etched, cylindrical pores are obtained. Figure 5-5A shows an SEM

of a correspondingly cylindrical Au nanowire plated within such a chemical-etch-only

membrane. (The wire has a bend in it near where it protrudes from the underlying

polycarbonate film.) The diameter of this exposed nanowire is 65 nm, in good agreement

with the 58 ± 6 nm value obtained for the pore diameter.
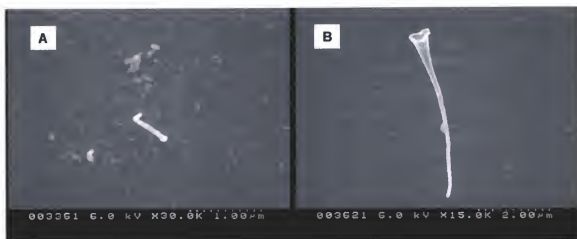
Figure 5-5. Scanning electron micrographs of the gold nanostructures plated into a
membrane that was not plasma etched and plasma etched. A) Not plasma
etched. B) Plasma etched for 5 minutes.
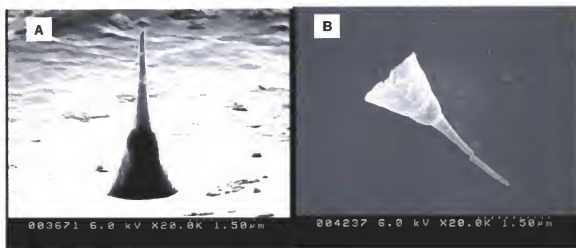
Figure 5-6. Two images of the conical gold nanostructures plated within a membrane
that had been plasma etched for 10 minutes. A) The polymeric membrane
material was removed with the tip of the nanostructure facing up. B) The
membrane material was removed with the tip of the nanostructure facing
down.

Figure 5-5B shows an analogous image of a Au nanostructure plated within a

membrane that had been chemically etched and then surface plasma etched for 5 min. As

expected this nanostructure is conical, in fact, trumpet-shaped. As per the schematic in

Figure 5-2, the base (or large diameter) of the cone is facing up in Figure 5-5B. The base

diameter is 640 nm, in good agreement with the 655-nm surface pore diameter (Figure 5-

3B) obtained for the O_2 plasma-etched membrane used to prepare this Au nanostructure.

Figure 5-7.   Scanning electron micrograph of a conical gold nanostructure plated within
a membrane that had been plasma etched for 15 minutes.

Figure 5-6 shows two images of conical Au nanostructures plated within a

membrane that had been chemically etched and then surface plasma etched for 10 min.

In Figure 5-6A the conical Au nanostructure is standing on its base with the tip facing up.

In Figure 5-6B the base of the conical Au nanostructure was facing up, but it has bent to

the left because the underlying tip cannot support the weight at the top. A comparison of

Figure 5-5B with Figure 6 shows that with increasing plasma-etch time, the pore goes

from a trumpet-like shaped to a funnel-like shape. That is, the plasma-widened part of

the pore extends deeper into the membrane as etch time increases. This is reinforced by

Figure 5-7, which shows a Au nanostructure plated within a membrane that had been

plasma etched for 15 min. The plasma-widened part of the pore (down in this image)

extends through most of the membrane thickness, and the pore looks more like a true cone.
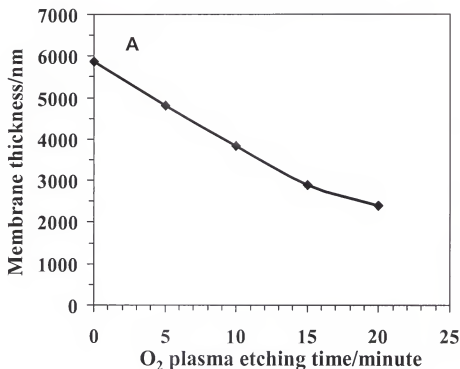
Figure 5-8. A) Plot of membrane thickness *vs.* plasma-etch time.

It is important to emphasize that regardless of plasma etch time there is a portion of the pore extending from the unetched surface that remains cylindrical with a pore diameter of 58 nm (see Figure 5-1C). We know this because SEM images of this face of the membrane show a pore diameter of 58 nm, regardless of plasma etch time. Further evidence for this unetched part of the pore is seen at the tips of the conical Au nanostructures plated within these pores (e.g., Figures 5-6A and 5-7). However, the length of this unetched cylindrical part of the pore decreases as the etch time increases. For membranes that were plasma etched for 6 min and 10 min, this remaining cylindrical part of the pore is ~ 0.4 μm and ~ 0.2 μm long, respectively. For longer etch times, the

remaining cylindrical part of the pore is too short to measure using the SEM methods developed here. We emphasize this point because this unetched part of the pore can be a contribution to pore's total ionic resistance.
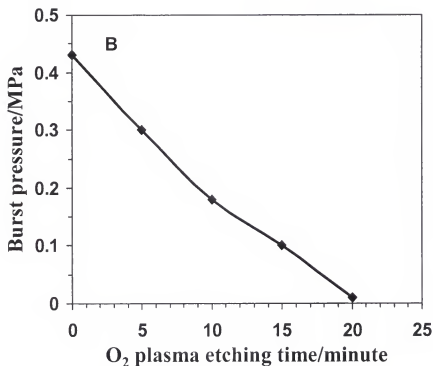
Figure 5- 8.   B) Plot of pressure required to burst the membrane *vs.* plasma etch time.

Membrane Thinning and Burst Strength

As illustrated in Figure 5-1C, the plasma etch process used to create the conical pores also thins the membrane. The relationship between membrane thickness and etch time (Figure 5-8A) was quantified by taking cross-sectional images of the membranes after various etch times. For example, after 20 minutes of etching the membrane was thinned from its initial thickness of 5.9 μm to 2.4 μm. Figure 5-8B shows the effect of membrane thinning on the mechanical properties of the membrane. The figure of merit here is the pressure of Ar required to burst the membrane. As would be expected, the pressure needed to burst the membrane decreases as the membrane is thinned. Etch times

longer than 20 minutes yielded membranes that were too fragile to be mounted in the U-tube cell.

Effect of Pore Shape on Membrane Resistance

As discussed in our previous work, the ionic resistance of an electrolyte-filled pore can be used as a convenient surrogate for the pore's mass-transfer resistance.[178] We have used an AC impedance experiment to obtain ionic resistance values for the membranes investigated here.[173] The objective of these experiments is to explore how pore shape affects membrane resistance and to demonstrate that conical-pore membranes can provide dramatically lower resistances than analogous cylindrical-pore membranes.

The resistance of an electrolyte-filled conical pore is given by

$$R_{con} = 4 \rho \, l_{con} / (\pi \, d_b \, d_t) \qquad (5\text{-}1)$$

where ρ is the resistivity of the electrolyte, l_{con} is the length of the pore (or equivalently the thickness of the membrane), and d_b and d_t are the diameters at the base and tip of the cone, respectively.[174] The resistance of an electrolyte-filled cylindrical pore is given by

$$R_{cyl} = 4 \rho \, l_{cyl} / (\pi \, d_{cyl}^2) \qquad (5\text{-}2)$$

where d_{cyl} is the diameter of the cylindrical pore, and l_{cyl} is the pore length or the membrane thickness. Rationing Equations 5-1 and 5-2 yields

$$R_{con} / R_{cyl} = l_{con} \, d_{cyl}^2 / l_{cyl} \, d_b \, d_t \qquad (5\text{-}3)$$

Equation 5-3 clearly demonstrates the transport advantage of a conical pore membrane. For example, Equation 3 predicts that a membrane containing conical pores with $d_b = 2.6$ μm, $d_t = 58$ nm, and $l_{con} = 2.4$ μm (similar to our membrane after 20 min of plasma etching) should have an ionic resistance that is two-orders of magnitude lower than the membrane before the plasma-etch treatment, where $d_{cyl} = 58$ nm and $l_{cyl} = 5.9$

μm. In fact, plasma etching has two advantages in this regard; it both widens the pore mouth ($d_b \gg d_{cyl}$) and thins the membrane ($l_{con} < l_{cyl}$).

However, as shown schematically in Figure 5-1C, and by the images in Figures 5-5 – 5-7, the pores in the plasma-etched membrane are not purely conical. Rather these pores have a segment of unetched cylindrical pore (down in Figure 5-1C) connected to the etched conical part of the pore; i.e. these membranes have an interesting cone-to-cylinder pore geometry. The resistance of an electrolyte-filled pore with this cone-to-cylinder geometry (R_{c-c}) is simply the series sum of the resistances of the cylindrical and conical parts.

$$R_{c-c} = 4 \rho \, l_{cyl} \, / \, (\pi \, d_{cyl}^2) \; + \; 4 \rho \, l_{con} \, / \, (\pi \, d_b \, d_t) \qquad (5\text{-}4)$$

As noted above, for intermediate etch times, the images of the plated Au nanostructures provide an estimate of the length of the unetched cylindrical part of the pore (l_{cyl} in Equation 5-4). This, and the known membrane thickness (Figure 5-8A), allow us to obtain an estimate for l_{con}, and Equation 5-4 can be used to calculate an approximate value of the ionic resistance of a pore with this cone-to-cylinder geometry.

We have used Equation 5-2 to calculate the resistance of the membrane contained cylindrical pores (no plasma-etch), Equation 5-4 to calculate the resistance of the membranes plasma etched for the intermediate times of 6 and 10 min (cylindrical-to-cone pore geometry). These equations give the resistance of a single pore (R_p) and since these pores are parallel to each other through the thickness of the membrane, the total membrane resistance (R_m) is given by

$$1/R_m = n/R_p \qquad (5\text{-}5)$$

where n is the number of pores in the membrane sample. We compare these calculated R_m values with experimental values obtained from the impedance data in Table 5-1.
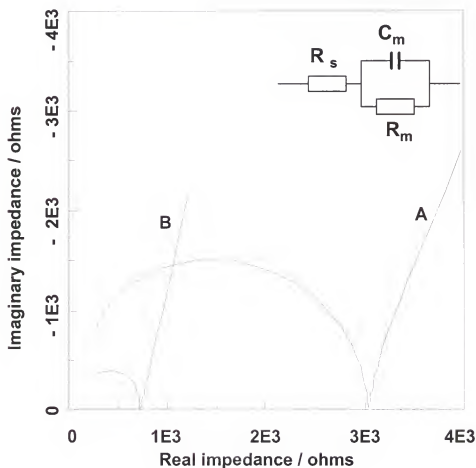
Figure 5-9. Nyquist plots for membranes plasma-etched for 6 and 10 minutes. A) 6 minutes of plasma etched membrane. B) 10 minutes of plasma etched membrane. The inset shows the equivalent circuit used to interpret the impedance data.

As per our prior work, the impedance data were interpreted in terms of the equivalent circuit shown in the inset of Figure 5-9.[173] In this circuit, R_s is the solution resistance, R_m is the membrane resistance, and C_m is the membrane capacitance. The

experimental impedance data (Nyquist plots, Figure 5-9) were fitted to curves simulated from this equivalent circuit using the Z-view curve-fitting software. The R_m values were obtained from the best-fit between the experimental and simulated Nyquist plots (Table 5-1).

Table 5-1. Experimental and calculated membrane resistance values.

Plasma etch time (min)	0	6	10	15	20
Experimental R_m (Ω)	~				
Calculated R_m (Ω)	5811^a	3520^b	2070^b	71^c	52^c

a. Calculated using Equation 5-2.
b. Calculated using Equation 5-4.
c. Calculated using Equation 5-1.

The experimental R_m values are in reasonable agreement with values calculated using either Equation 5-1, 5-2 or 5-4. The agreement is especially good for long etch times because the pores in this membranes more closely approximate ideal cones. This eliminates the need to have a good experimental value for the length of the residual cylindrical part of the pore; i.e., Equation 5-1 instead of Equation 5-4 can be used to calculate the membrane resistance. For the intermediate etch times (6 and 10 min), where Equation 5-4 must be used, the calculated R_m values are larger than the experimental values. This reflects the importance of the residual cylindrical part of the pore in determining the pore resistance. The calculated values are too large because apparently our SEM method used to obtain the length of the residual cylindrical part over estimates the length and/or underestimates the diameter of this part of the pore.

We do not show an experimental R_m value for the cylindrical pore (no plasma-etch) membrane in Table 5-1 because we had difficulty in getting the pores to wet, even with the use of the PVP wetting agent. As a result, the membrane resistance was always

orders of magnitude higher than the calculated value and was not reproducible. The plasma etch method has yet another interesting advantage in that it increases the hydrophilicity of the membrane surface.[176] This was proven using water-droplet contact-angle measurements. The contact angle of the chemically, but not plasma-, etched membrane was 74°, while the contact angle for the 15min and 20 min plasma-etched membrane was 6°. As a result we had no difficulty in wetting the pores in the plasma-etched membranes. It is also interesting to note that Equation 5-3 predicts that the resistance of the membrane etched for 20 minutes should be two-orders of magnitude lower than that of the corresponding cylindrical-pore membrane, and this is exactly what is observed experimentally (Table 5-1).

Finally, a track-etch filter with cylindrical pores having the same diameter (55 ± 5 nm) as the cylindrical part of the pores in the membrane studied here (58 nm) is commercially available.[178] However, this commercial membrane has a pore density that is four orders of magnitude higher than the membranes used here. The resistance of the commercial membrane was determined using the same apparatus and AC impedance method used for the conical-pore membranes; a value of 2 Ω was obtained. Hence, in spite of its enormously higher pore density, the resistance of this commercial cylindrical pore membrane is only a factor of 20 smaller than our best conical-pore membrane (Table 5-1). These data clearly demonstrate the power of the conical-pore approach for reducing membrane resistance.

Conclusions

We have demonstrated a simple plasma-etch method for converting cylindrical pores in a polymeric membrane into conical pores. This method allows for a great deal

of control over the shape of the resulting pores. Short plasma-etch times yield pores that are cylindrical through most of the membrane thickness, but "blossom" into cones at one membrane face (Figure 5-5B). Long etch times yield nearly perfectly conical pores (Figure 5-7). We have used an AC impedance method to demonstrate an important advantage of converting the cylindrical pores into conical pores – the membrane resistance can be dramatically reduced. Indeed, our best conical pore membrane has an ionic resistance that is within a factor of 20 of that of a comparable commercial membrane with cylindrical pores, even though the commercial membrane has a four-order-of-magnitude higher pore density.

A final point is worth making in this regard. The chemical species used to determine the resistance values for these membranes (Na^+ and Cl^-) have negligible size relative to the dimensions of any of the pores studied here. If instead we were interested in optimizing the flux of a macromolecule (e.g. a protein) whose diameter is comparable to the diameter of the cylindrical pore,[119] then the conical-pore approach would have even greater advantage. This is because when the pore and the molecule being transported are of comparable dimensions, the diffusion coefficient within the pore plummets relative to the bulk-solution value – hindered diffusion.[115] In the cylindrical pore, hindered diffusion would occur down the entire length of the pore. In contrast, in the conical pore, hindered diffusion would only occur at the cone tip. As a result, the flux of the protein molecule would be dramatically higher in the conical pore. Hence, for large permeate molecules our best low pore-density conical-pore membrane should yield higher fluxes than the commercial membrane, in spite of its higher porosity. We are currently

exploring this issue and the general issue of transport selectivity in these conical-pore membranes.

CHAPTER 6
CONCLUSIONS

Template synthesis is a general method to prepare nanomaterials. In this research, this method was used to prepare SnO_2 nanofibers and nanoporous carbon-honeycomb, which were used as Li-ion battery anodes. Both electrodes showed improved rate capability and cycling performance compared with the conventional thin-film electrodes having the same mass. Improved rate capabilities were obtained because the distance over which Li^+ must diffuse in the solid state was dramatically decreased in the nanostructured electrodes. Furthermore, the surface area of the nanostructured electrode was larger, making the effective current-density during discharge smaller than that for a conventional electrode. Better cycling performance was achieved because there were spaces between the nanostructures of electrode materials, and such spaces could accommodate the volume changes due to Li^+ insertion and extraction through the electrode materials.

In addition to the use as Li-ion battery anode, the nanostructured carbon honeycomb was also investigated to make a nanostructured all-solid-state Li-ion battery, which can combine the advantages of both nanostructured electrodes and the all-solid-state Li-ion battery. In this approach, the carbon honeycomb was used as the anode and the substrate; then, solid electrolyte thin film was deposited onto the surface and the inner walls of carbon honeycomb; finally the resulted electrolyte nanotubes could be filled with cathode nanofibers. Electropolymerized poly(phenylene oxide) (PPO) thin film was prepared and used as solid electrolyte. PPO was impermeable for both positively and

86

negatively charged ions. However, after sulfonation, PPO was conductive only to the positively charged ion but not to the negatively charged ion. This is because after sulfonation, PPO was negatively charged, and the electrical attraction could enhance the transport of positively charged ion through the negatively charged PPO film.

In this research, O_2 plasma etching was used to prepare not only carbon honeycomb but also nanostructured conical pores. It demonstrated that O_2 plasma etching was a very simple technique to prepare conical pore embedded polycarbonate membranes without the use of corrosive solution. After polycarbonate membranes were etched from one side by O_2 plasma, the pore diameter of this side was increased; while that on the other side was unchanged. With the increase of plasma etching time, the thickness and strength of membranes were decreased, and the pore structure was changed from the monodisperse cylindrical shape to triumph-like shape, and then changed to funnel-shape. The conical pore embedded membranes showed dramatic increase in membrane transport compared with cylindrical pore embedded membranes.

LIST OF REFERENCES

1. K. J. Klabunde, in *Nanoscale Materials in Chemistry*, Wiley-Interscience, New York (2001).

2. C. R. Martin and D. T. Mitchell, *Anal. Chem.*, **70**, 322A (1998).

3. C. R. Martin, *Science*, **266**, 1961 (1994).

4. T. M. S. Chang and S. Prakash, *Mol. Biotechnol.*, **17**, 249 (2001).

5. C. Kneuer, *Bioconjug. Chem.*, **11**, 926 (2000).

6. J. O. Radler, I. Koltover, T. Salditt, and C. R. Safina, *Science*, **275**, 810 (1997).

7. I. Koltover, T. Salditt, J. O. Radler, and C. R. Safina, *Science*, **281**, 78 (1998).

8. Y. Cao, R. Jin, and C. A. Mirkin, *Science*, **297**, 1536 (2002).

9. L. M. Demers, *Science*, **296**, 1836 (2002).

10. S. J. Park, T. A. Taton, and C. A. Mirkin, *Science*, **295**, 1503 (2002).

11. K. E. Ulrich, S. M. Cannizzaro, R. S. Langer, and K. M. Shakeshelf, *Chem. Rev.*, **99**, 3181 (1999).

12. K. E. Lee, B. K. Kim, and S. H. Yuk, *Biomacromolecules*, **3**, 1115 (2002).

13. N. Murthy, Y. X. Schuck, M. Xu, and J. M. Frechet, *J. Am. Chem. Soc.*, **124**, 12398 (2002).

14. J. P. Linsky, T. R. Paul, and M. Kenny, *J. Polym. Sci.*, **A-29**, 143 (1971).

15. P. Yager and P. Schoen, *Mol. Cryst. Liq. Cryst.*, **106**, 371 (1984).

16. J. M. Schnur, *Science*, **262**, 1669 (1993).

17. J. V. Sellinger, M. S. Spector, and J. M. Schnur, *J. Phys. Chem. B*, **105**, 7157 (2001).

18. R. Price and M. Patchan, *J. Microencapsul.*, **8**, 301 (1991).

19. A. S. Goldstein, *Bioorg. Med. Chem.*, **9**, 2819 (2001).

20. S. Iijima, *Nature*, **352**, 56 (1991).

21. P. M. Alayan, in *Carbon Nanotubes: Preparation and Properties*, T. W. Ebbesen Editor, Ch. 3, CRC Press, Cleveland, Ohio (1997).

22. P. M. Ajayan, *Chem. Rev.*, **99**, 1787 (1999).

23. H. Dai, *J. Am. Chem. Soc.*, **103**, 11246 (1999).

24. D. T. Mitchell, *J. Am. Chem. Soc.*, **124**, 11864 (2002).

25. S. B. Lee, *Science*, **296**, 2198 (2002)

26. M. Nishizawa, V. P. Menon, and C. R. Martin, *Science*, **296**, 2198 (2002).

27. K. B. Jirage, J. C. Hulteen, and C. R. Martin, *Science*, **278**, 655 (1997).

28. M. R. Ghaadiri, J. R. Granja, R. A. Milligan, D. E. McRee, and N. Khazanovich, *Nature*, **366**, 324 (1993).

29. N. Khazanovich, J. R. Granja, D. E. McRee, R. A. Milligan, and M. R. Ghadiri, *J. Am. Chem. Soc.*, **116**, 6011 (1994).

30. S. Fernandez-Lopez, *Nature*, **412**, 452 (2001).

31. M. R. Ghdiri, J. R. Granja, and L. K. Buehler, *Nature*, **369**, 301 (1994).

32. R. Chen, Y. Zhang, D. Wang, and H. Dai, *J. Am. Chem. Soc.*, **123**, 3838 (2001).

33. B. R. Azamian, J. J. Davis, K. S. Coleman, C. B. Bagshaw, and M. L. H. Creen, *J. Am. Chem. Soc.*, **124**, 12664 (2002).

34. B. F. Erlanger, B. Chen, M. Zhu, and L. Brus, *Nano Letters*, **1**, 465 (2001).

35. M. Shim, N. Kam, R. Chen, Y. Li, and H. Dai, *Nano Letters*, **2**, 285 (2002).

36. S. S. Wang, E. Joselevich, A. T. Woolley, C. Cheung, and C. M. Lieber, *Nature*, **394**, 52 (1998).

37. M. Jacoby, *Chem. Eng. News*, **80**, 38 (2002).

38. T. Rueckes, *Science*, **289**, 94 (2000).

39. A. Bachtold, P. Hadley, T. Nakanishi, and C. Dekker, *Science*, **294**, 1317 (2001).

40. J. C. Hulteen and C. R. Martin, *J. Mater. Chem.*, **7**, 1075 (1997)

41. G. L. Hormyak, C. J. Patrissi, and C. R. Martin, *J. Phys. Chem. B*, **101**, 1548 (1997).

42. G. E. Possin, *Rev. Sci. Instrum.*, **41**, 772 (1970).

43. W. D. Williams and N. Giordano, *Rev. Sci. Instrum.*, **55**, 410 (1984).

44. J. C. Hulteen, K. B. Jirage, and C. R. Martin, *J. Am. Chem. Soc.*, **120**, 6603 (1998).

45. K. B. Jirage, J. C. Hulteen, and C. R. Martin, *Anal. Chem.*, **71**, 4913 (1999).

46. Z. Hou, N. L. Abbott, and P. Stroeve, *Langmuir*, **16**, 2401 (2000).

47. G. Tourillon, L. Pontinnier, J. P. Levy, and V. Langlais, *Electrochemical and Solid-State Letters*, **3**, 20 (2000).

48. C. Schonenberger, B. M. I. Van der Zande, L. G. J. Fokkink, M. Henry, C. Schmid, M. Kruger, A. Bachtold, R. Huber, H. Birk, and U. Staufer, *J. Phys. Chem. B.*, **101**, 5497 (1997).

49. C. K. Preston and M. J. Moskovits, *J. Phys. Chem. B.*, **97**, 8405 (1997).

50. C. R. Martin, in *Handbook of Conductive Polymers*, J. R. Reynolds, T. Skotheim, R. Elsebaumer, and M. Dekker, Editors, 2nd ed., p. 409, New York (1997).

51. J. Duchet, R. Legras and S. Demoustier-Champagne, *Synthetic Metals*, **98**, 113 (1998).

52. S. Demoustier-Champagne and P. Y. Stavaaux, *Chem. Mater.*, **11**, 829 (1999).

53. S. Sukeerthi and Q. Contractor, *Anal. Chem.*, **71**, 2231 (1999).

54. B. B. Lakshmi, C. J. Patrissi, and C. R. Martin, *Chem. Mater.*, **9**, 2544 (1997).

55. B. B. Lakshmi, P. K. Dorhout, and C. R. Martin, *Chem. Mater.*, **9**, 857 (1997).

56. G. Che, B. B. Lakshmi, C. R. Martin, and E. R. Fisher, *Langmuir*, **15**, 750 (1999).

57. G. Che, E. R. Fisher, and C. R. Martin, *Nature*, **393**, 346 (1998).

58. T. Kyotani, L. F. Tsai, and A. Tomita, *Chem. Commun.*, **19**, 701 (1997).

59. C. J. Patrissi and C. R. Martin, *J. Electrochem. Soc.*, **146**, 3176 (1999).

60. N. Li, C. J. Patrissi, and C. R. Martin, *J. Electrochem. Soc.*, **147**, 2044 (2000).

61. G. Che, K. B. Jirage, E. R. Fisher, C. R. Martin, and H. Yoneyama, *J. Electrochem. Soc.*, **144**, 4296 (1997).

62. V. M. Cepak, J. C. Hulteen, G. Che, K. B. Jirage, B. B. Lakshmi, E. R. Fisher, and C. R. Martin, *J. Mater. Res.*, **13**, 3070 (1998).

63. V. M. Cepak, J. C. Hulteen, G. Che, K. B. Jirage, B. B. Lakshmi, E. R. Fisher, and C. R. Martin, *Chem. Mater.*, **9**, 1065 (1997).

64. B. R. Martin, D. J. Dermody, B. D. Reiss, M. Fang, L. A. Lyon, M. J. Natan, and T. E. Mallouk, *Adv. Mater.*, **11**, 1021 (1999).

65. C. Wu and T. Bein, *Science*, **264**, 1757 (1994).

66. R. L. Fleischer, P. B. Price and R. M. Walker, in *Nuclear Tracks in Solids*, University of California Press, Berkeley, CA (1975).

67. M. Wirtz, S. Yu, and C. R. Martin, *Analyst*, **127**, 871 (2002).

68. A. Despic and V. P. Parkhuitik, in *Modern Aspects of Electrochemistry*, J. O. Bockris, R. E. White and B. E. Conway, Editors, Plenum Press, Vol. 20, Ch. 6, Plenum Press, New York (1989).

69. C. A. Foss, Jr., G. L. Hornyak, J. A. Stockert, and C. R. Martin, *J. Phys. Chem.*, **98**, 2963 (1994).

70. C. A. Foss, Jr., G. L. Hornyak, J. A. Stockert, and C. R. Martin, *Adv. Mater.*, **5**, 135 (1993).

71. R. J. Tonucci, B. L. Justus, A. J. Campillo, and C. E. Ford, *Science*, **258**, 783 (1992).

72. J. S. Beck, J. C. Vartuli, W. J. Roth, M. E. Leonowicz, C. T. Kresge, K. D. Schmitt, C. Chu, D. H. Olson, E. W. Sheppard, S. B. McCullen, J. B. Higgins, and J. L. Schlenker, *J. Am. Chem. Soc.*, **114**, 10834 (1992).

73. K. Douglas, G. Devaud, and N. A. Clark, *Science*, **257**, 642 (1992).

74. T. D. Clark and M. R. Ghadiri, *J. Am. Chem. Soc.*, **117**, 12364 (1995).

75. G. A. Ozin, *Adv. Mater.*, **4**, 612 (1992).

76. R. Schollhorn, *Chem. Mater.*, 8, 1747 (1996).

77. V. P. Menon and C. R. Martin, *Anal. Chem.*, **67**, 1920 (1995).

78. M. S. Kang and C. R. Martin, *Langmuir*, **17**, 2753 (2001).

79. S. B. Lee and C. R. Martin, *Anal. Chem.*, **73**, 768 (2001).

80. W. J. Petzny and J. A. Quinn, *Science*, **166**, 751 (1969).

81. C. R. Martin, M. Nishizawa, K. B. Jirage, and M. S. Kang, *J. Phys. Chem. B*, **105**, 1925 (2001).

82.   M. Wakihara, *Materials science and Engineering R-Reports*, **33**, 109 (2001).

83.   P. Arora and V. Srinivasan, *J. Electrochem. Soc.*, **149**, K1 (2002).

84.   D. R. Sadoway and A. M. Mayes, *MRS Bulletin*, **27**, 590 (2002).

85.   T. Nagaura and K. Tazawa, *Progr. Batteries and Solar Cells*, **9**, 20 (1990).

86.   Y. Idota, T. Kubota, A. Matsufuji, Y. Maekawa, and T. Miyasaki, *Science*, **276**, 1395 (1997).

87.   J. O. Besenhard, J. Yang, and M. Winter, *J. Power Sources*, **68**, 87 (1997).

88.   I. A. Courtney and J. R. Dahn, *J. Electrochem. Soc.*, **144**, 2045 (1997).

89.   A. Yamada, S. C. Chung, and K. Hinokuma, *J. Electrochem.* Soc., **148**, A224 (2001).

90.   M. M. Doeff, A. Anaplosky, L. Edman, T. J. Richardson, and L.C. De Jonghe, *J. Electrochem. Soc.*, **148**, A230 (2001).

91.   A. Yamada, Y. Kudo, and K. Liu, *J. Electrochem. Soc.*, **148**, A747 (2001).

92.   H. Huang and S. Wunder, *J. Electrochem. Soc.*, **148**, A279 (2001).

93.   F. Croce, G. B. Appetecchi, L. Persi, and B. Scrosati, *Nature*, **394**, 456 (1998).

94.   M. C. Smart, B. V. Ratnakumar, and S. Surampudi, *J. Electrochem. Soc.*, **146**, 486 (1999).

95.   P. G. Bruce, *Chem. Commun.*, **19**, 1817 (1997).

96.   R. Moshtev and B. Johnson, *J. Power Sources*, **91**, 86 (2000).

97.   H. Li, L. Shi, W. Lu, X. Huang, and L. Chen, *J. Electrochem. Soc.*, **148**, A915 (2001).

98.   L. Y. Beaulieu, D. Larcher, R. A. Dunlap, and J. R. Dahn, *J. Electrochem. Soc.*, **147**, 3206 (2000).

99.   G. Maurin, F. Henn, B. Simon, J. F. Colomer, and J. B. Nagy, *Nano Letters*, **1**, 75 (2001).

100.   I. Mukhopadhyay, N. Hoshino, S. Kawasaki, F. Okino, W. K. Hsu, and H. Touhara, *J. Electrochem. Soc.*, **149**, A39 (2002).

101.   M. E. Spahr, P. Stoschitzki-Bitterli, R. Nespar, O. Hass, and P. Novak, *J. Electroche*m. Soc., **146**, 2780 (1999).

102.   J. S. Sakamoto and B. Dunn, *J. Electrochem. Soc.*, **149**, A26 (2002).

103.   D. Le, S. Passerini, J. Guo, J. Ressler, B. B. Owens, and W. H. Smyrl, *J. Electrochem. Soc.*, **143**, 2099 (1996).

104.   M. J. Parent, S. Passerini, B. B. Owens, and W. H. Smyrl, *J. Electrochem. Soc.*, **146**, 1346 (1999).

105.   H, Bayley and C. R. Martin, *Chem. Rev.*, **100**, 2575 (2000).

106.   R. W. Lines, in *Particle Size Analysis*, N. G. Stanley-Wood and R. W. Lines Editors, Royal Society of Chemistry, London (1992)

107.   H. E. Kubitschek, in *Methods in Microbiology*, J. R. Norris and D. W. Ribbons, Editors, Elsevier Science & Technology Books, New York (1979).

108.   S. B. Hladky and D. A. Haydon, *Nature*, **225**, 451 (1970).

109.   H. Bayley, *Curr. Opin. Biotechnol.*, **10**, 94 (1999).

110.   H. Bayley and P. S. Cremer, *Nature*, **413**, 226 (2001).

111.   J. Sanchez-Quesada, M. R. Ghadiri, H. Bayley, and O. Braha, *J. Am. Chem. Soc.*, **122**, 11757 (2000).

112.   R. V. Parthasarathy, V. P. Menon and C. R. Martin, *Chem. Mater.*, **9**, 560 (1997).

113.   W. Chen and C. R. Martin, *J. Membr. Sci.*, **104**, 101 (1995).

114.   C. Liu and C. R. Martin, *Nature*, **352**, 50 (1991).

115.   V. M. Deen, *AICHE J.*, **33**, 1409 (1987).

116.   I. A. Kathawalla, J. L. Anderson and J. S. Lindsey, *Macromolecules*, **22**, 1215 (1989).

117.   J. M. Nitsche and G. Balgi, *Ind. Eng. Chem. Res.*, **33**, 2242 (1994).

118.   S. B. Lee and C. R. Martin, *J. Am. Chem. Soc.*, **124**, 11850 (2002).

119.   S. Yu, S. B. Lee, and C. R. Martin, *Anal. Chem.*, **75**, 1239 (2003).

120.   T. D. Tran, J. H. Feikert, R. W. Pekala, and K. Kinoshita, *J. Appl. Elctrochem.*, **26**, 161 (1996).

121.   G. S. Nagarajan, J. W. Van Zee, and R. W. Spotnitz, *J. Electrochem. Soc.*, **145,** 771 (1998).

122. J. M. Tarascon, E. Wang, F. K. Shokoohi, W. R. McKinnon, and S. Colson, *J. Electrochem. Soc.,* **138**, 2859 (1991).

123. A. L. Tipton, S. Passerini, B. B. Owens, and W. H. Smyrl, *J. Electrochem. Soc.,* **143**, 3473 (1996).

124. Y. Idota, M. Mishima, M. Miyaki, T. Kubota, and T. Miyasaka, *Eur. Pat. Appl.,* 65140 A1 94116643.1 (1994).

125. K. Tahara, H. Ishikawa, F. Iwasaki, S. Yahagi, A. Sakkata, and T. Sakai, *Eur. Pat. Appl.,* 93111938.2 (1993).

126. J. Isidorsson, C. G. Granqvist, L. Haggstrom, and E. Nordstrom, *J. Appl. Phys.,* **80**, 2367 (1996).

127. V. M. Cepak and C. R. Martin, *J. Phys. Chem. B,* **102**, 9985 (1998).

128. C. Schonenberger, B. M. I. van der Zane, L. G. J. Fokkink, M. Henry, C. Schmid, M. Kruger, A. Bachtold, R. Huber, H. Birk, and U. Staufer, *J. Phys. Chem. B,* **101**, 5497 (1997).

129. Joint Commission on Powder Diffraction Standards, International Center for Diffraction Data, File 41-1445.

130. T. Brousse, R. Retoux, U. Herterich, and D. M. Schleich, *J. Electrochem. Soc.,* **145**, 1 (1998).

131. S. Panero, G. Savo, and B. Scrosati, *Electrochemical and Solid-State Letters,* **2**, 365 (1999).

132. I. A. Courtney and J. R. Dahn, *J. Electrochem. Soc.,* **144**, 2943 (1997).

133. E. Peled, *J. Electrochem. Soc.,* **126**, 2047 (1979).

134. A. H. Whitehead, J. M. Elliott, and J. R. Owen, *J. Power Sources,* **81-82**, 33 (1999).

135. B .A. Johnson and R. E. White, *J. Power Sources,* **70**, 48 (19997).

136. G. Nagasubraamanian and R. G. Jungst, *J. Power Sources,* **72**, 189 (1998).

137. G. Nagasubraamanian, *J. Appl. Electrochem.,* **31**, 99 (2001).

138. K. Zaghib, F. Broachu, A. Guerfi, and K. Kinoshita, *J. Power Sources,* **103**, 140 (2001).

139. H. Masuda, M. Watanabe, K. Yasui, D. Tryk, T. Rao, and A. Fujishima, *Adv. Mater. (weinheim, Ger.),* **12**, 444 (2000).

140.   H. Masuda and M. Satoh, *Jpn. J. Appl. Phys. Part 1*, **35**, L126 (1996).

141.   R. C. Furneaux, W. R. Rigby, and A. P. Davidson, *Nature* (London), **337**, 147 (1989).

142.   S. A. Miller, V. Y. Young, and C. R. Martin, *J. Am. Chem. Soc.*, **123**, 12335 (2001).

143.   D. Aurbach, J. S. Gnanaraj, M. D. Levi, E. D. Levi, J. E. Fisher, and A. Claye, *J. Power Sources*, **97-98**, 92 (2001).

144.   J. S. Gnanaraj, M. D. Levi, E. Levi, G. Salitra, D. Aurbach, J. E. Fisher, and A. Claye, *J. Electrochem. Soc.*, **148**, A525 (2001).

145.   A. Johansson and J. Carlsson, *Thin Solid Films*, **261**, 52 (1995).

146.   E. Peled, C. Menachem, D. Bar-Tow, and A. Melman, *J. Electrochem. Soc.*, **143**, L4 (1996).

147.   Y. Ein-Eli and V. R. Koch, *J. Electrochem. Soc.*, **144**, 2968 (1997).

148.   G. Beamson and D. Briggs, in *High Resolution XPS of Organic Polymers*, p. 152, 180, John Wiley & Sons, New York (1992).

149.   C. D. Waganer, A. V. Naumkin, A. Kraut-Vass, J. W. Allison, C. J. Powell and J. R. Rumble, Jr.,in *NIST X-ray Photoelectron Spectroscopy Database, Standard Reference Database 20*, version 3.2 (Web Version), U.S. Secretary of Commerce, 2000.

150.   D. Bar-Tow, E. Peled, and L. Burstein, *J. Electrochem. Soc.*, **146**, 824 (1999).

151.   R. J. Brodd, the Electrochemical Society *Interface*, **Fall**, 20 (1999).

152.   G. Halpert, H. Frank, and S. Surampudi, the Electrochemical Society *Interface, **Fall**, 25 (1999).

153.   C. F. Holmes, the Electrochemical Society *Interface*, **Fall**, 32 (1999).

154.   T. Uchida, Y. Morikawa, H. Ikuta, and M. Wakihara, *J. Electrochem. Soc.*,**143**, 2606 (1996).

155.   M. Nishizawa, R. Hashitani, T. Itoh, T. Matsu, and I. Uchida, *Electrochemical and Solid-State Letters*, **1**, 10 (1998).

156.   P. Olivi, E. C. Pereira, E. Longo, J. A. Vare, and L. O. Bulhoes, *J. Electrochem. Soc.*,**140**, L81 (1993).
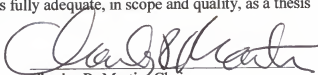
157. K. Dokko, M. Nishizawa, M. Mohamedi, M. Umeda, I. Uchida, J. Akimoto, Y. Takahashi, Y. Gotoh, and S. Mizuta, *Electrochemical and Solid-State Letters*, **4**, A151 (2001).

158. Y. Jang, B. J. Neudecker, and J. Dudney, *Electrochemical and Solid-State Letters*, **4**, A74 (2001).

159. M. D. Levi, Z. Lu, and D. Aurbach, *J. Power Sources*, **97-98**, 482 (2001).

160. J. B. Bates, D. Lubben, N. J. Dudney, and F. X. Hart, *J. Electrochem. Soc.*, **142**, L149 (1995).

161. J. B. Bates, G. R. Gruzalski, N. J. Dudney, and X, Yu, *Solid State Ionics*, **70/71**, 619 (1994).

162. E. Jeon, Y. Shin, S. Nam, W. Cho, and Y. Yoon, *J. Electrochem. Soc.*, **148**, A318 (2001).

163. S. Lee, P. Liu, C. E. Tracy, and D. K. Benson, *Electrochemical and Solid-State Letters.*, **2**, 425 (1999).

164. M. Baba, N. Kumagai, H. Kobayashi, OL Nakano, and K. Nishidate, *Electrochemical and Solid-State Letters*, **2**, 320 (1999).

165. Y. Park, S. Lee, B. Lee, and S. Joo, *Electrochemical and Solid-State Letters*, **2**, 58 (1999).

166. X. Yu, J. Bates, G. E. Jellison, and F. X. Hart, *J. Electrochem. Soc.*, **144**, 524 (1997).

167. B. Scrosati, in *Lithium Ion Batteries – Fundamentals and Performance*, M. Wakihara and O. Yamamoto, Editors, p. 220, Wiley-Vch, New York (1998).

168. R. L. McCarley, R. E. Thomas, E. A. Irene and R. W. Murray, *J. Electroanal. Chem.*, **290**, 79 (1990).

169. M. Gattrell and D. W. Kirk, *J. Electrochem. Soc.*, **140**, 903 (1993).

170. C. J. Powell and A. Jablonski, in *NIST Electron Effective-Attenuation-Length Database* – Version 1.0, National Institute of Standards and Technology, Gaithersburg, MD (2001).

171. Y. Kobayashi and C. R. Martin, *Anal. Chem.*, **71**, 3665 (1999).

172. P. Ugo, L. M. Moretto, S. Bellomi, V. P. Menon, and C.R. Martin, *Anal. Chem.*, **68**, 4160 (1996).

173. E. D. Steinle, D. T. Mitchell, M. Wirtz, S. B. Lee, V. Y. Young, and C. R. Martin, *Anal. Chem.*, **74**, 2416 (2002).

174. P. Y. Apel, Y. E. Korchev, Z. Siwy, R. Spohr and M. Yoshida, *Nuclear Instruments and Methods in Physics Research B,* **184**, 337 (2001).

175. I. Cheng, L. D. Whiteley, and C. R. Martin, *Anal. Chem.*, **61**, 762 (1989).

176. S. N. Dmitriev, L. I. Kravets, and V. V. Sleptsov, *Nuclear Instruments and Methods in Physics Research B*, **142**, 43 (1998).

177. S. Yu, N. Li, J. Wharton, and C. R. Martin, *Nano Letters*, **3**, 815 (2003).

178. G. Rahela and C. R. Martin, *Electrochimica Acta*, in press.

BIOGRAPHICAL SKETCH

Naichao Li was born in Zhangqiu, Shandong, China; the fourth child in the family of General Keguan Li and Guangxia Zou. He moved with his family to Nenjiang, Heilongjiang, China where he graduated from high school. Naichao developed an interest in chemistry at an early age, when he was doing his chemistry experiments in high school. This interest continued through college at Harbin Institute of Technology (HIT), China, where he majored in applied chemistry with an emphasis in electrochemical engineering. After graduating with a M.S. degree from HIT, he worked in Dalian Institute of Chemical Physics, Chinese Academy of Sciences for 9 years. He then went to the Department of Chemistry at the University of Florida to pursue his Ph.D. degree. Outside science, Naichao enjoys spending time with his wife Jing Sun and son Xingyue Li.

I certify that I have read this study and that in my opinion it conforms to acceptable standards of scholarly presentation and is fully adequate, in scope and quality, as a thesis for the degree of Doctor of Philosophy.
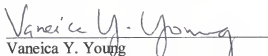
Charles R. Martin, Chair
Professor of Chemistry

I certify that I have read this study and that in my opinion it conforms to acceptable standards of scholarly presentation and is fully adequate, in scope and quality, as a thesis for the degree of Doctor of Philosophy.

Weihong Tan
Professor of Chemistry

I certify that I have read this study and that in my opinion it conforms to acceptable standards of scholarly presentation and is fully adequate, in scope and quality, as a thesis for the degree of Doctor of Philosophy.
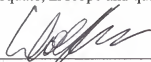
Vaneica Y. Young
Associate Professor of Chemistry

I certify that I have read this study and that in my opinion it conforms to acceptable standards of scholarly presentation and is fully adequate, in scope and quality, as a thesis for the degree of Doctor of Philosophy.

Daniel R. Talham
Professor of Chemistry

I certify that I have read this study and that in my opinion it conforms to acceptable standards of scholarly presentation and is fully adequate, in scope and quality, as a thesis for the degree of Doctor of Philosophy.

Wolfgang M. Sigmund
Associate Professor of Materials Science and Engineering

This dissertation was submitted to the Graduate Faculty of the Department of English in the College of Liberal Arts and Sciences and to the Graduate School and was accepted as partial fulfillment of the requirements for the degree of Doctor of Philosophy.

December, 2003

_____

Dean, Graduate School